ABSTRACT

Title of Document: Design and Characterization of p-i-n Devices for Betavoltaic Microbatteries on Gallium Nitride

Muhammad Raziuddin A. Khan, Masters of Science in Electrical Engineering 2015

Directed By: Dr. Agis Iliadis, Electrical and Computer Engineering Department

Betavoltaic microbatteries convert nuclear energy released as beta particles directly into electrical energy. These batteries are well suited for electrical applications such as micro-electro-mechanical systems (MEMS), implantable medical devices and sensors. Such devices are often located in hard to access places where long life, micro-size and lightweight are required. The working principle of a betavoltaic device is similar to a photovoltaic device; they differ only in that the electron hole pairs (EHPs) are generated in the device by electrons instead of photons.

In this study, the performance of a betavoltaic device fabricated from gallium nitride (GaN) is investigated for beta particle energies equivalent to Tritium ($^{3}H$) and Nickel-63 ($N^{63}$) beta sources. GaN is an attractive choice for fabricating betavoltaic devices due to its wide band gap and radiation resistance. Another advantage GaN has is that it can be alloyed with aluminum (Al) to further increase the bandgap, resulting in a higher output power and increased efficiency.

Betavoltaic devices were fabricated on *p-i-n* GaN structures grown by metalorganic chemical vapor deposition (MOCVD). The devices were characterized using current - voltage (IV) measurements without illumination (light or beta), using a laser driven light source, and under an electron beam. Dark IV measurements

showed a turn on-voltage of ~ 3.4 V, specific-on-resistance of 15.1 m $\Omega$-cm$^2$, and a leakage current of 0.5 mA at – 10 V. A clear photo-response was observed when IV curves were measured for these devices under a light source at a wavelength of 310 nm (4.0 eV). These devices were tested under an electron beam in order to evaluate their behavior as betavoltaic microbatteries without using radioactive materials. Output power of 70 nW and 640 nW with overall efficiencies of 1.2% and 4.0% were determined at the average energy emission of $^{3}$H (5.6 keV) and $^{63}$N (17 keV) respectively.

# DESIGN AND CHARACTERIZATION OF P-I-N DEVICES FOR BETAVOLTAIC MICROBATTERIES ON GALLIUM NITRIDE

By

Muhammad Raziuddin A. Khan.

Thesis submitted to the Faculty of the Graduate School of the
University of Maryland, College Park, in partial fulfillment
of the requirements for the degree of
Masters of Science
2015

Advisory Committee:
Dr. Agis A. Iliadis, Chair
Dr. Kenneth A. Jones
Dr. Robert W. Newcomb

*To my parents and my brothers (5)*

# Acknowledgements

First of all, I want to thank the Almighty Allah for giving me the strength and guidance to complete this work.

I would like to sincerely thank and express my deepest gratitude to Dr. Kenneth A. Jones, Dr. Joshua R. Smith and Dr. Randy P. Tompkins: Dr. Jones for giving me the opportunity to work under his guidance at the US Army Research Laboratory. As my supervisor at ARL and a committee member, he's not only arranged the funding necessary for this research work, but also guided me through the writing process and was always available to answer my questions. Joshua and Randy for their mentorship and guidance through all aspects of this research work at ARL. They guided me through the day-to-day research work and played a huge role in my professional development over the past two years. I have learned a lot from them for which I am grateful.

I would also like to thank my thesis adviser, Dr. Agis A. Iliadis for his supervision and support on this project. His insight and enjoyment of solid state physics, which was apparent in his classes, persuaded me to choose a career in the solid state arena. A special thanks to Dr. Robert W. Newcomb for gracefully accepting to be on my thesis committee.

I would also like to thank our collaborator at SUNY Albany for growing the GaN samples, Steven Kelley for making the electron beam measurements, Joshua for making EBIC measurements, and others who has assisted with this research work: Mike Derange, Jeremy, Tom Laughran, and Kevin Kirchner.

I would also like to thank all my friends and family for their unconditional support, love and encouragement.

# Table of Contents

# List of Figures

# Chapter 1. Introduction

The United States military needs batteries which have long lifetime, are lightweight and can function in extreme environments. They need these batteries to power sensors and other electronic devices placed in remote locations, where minimum maintenance and long lifetime are required. Microelectromechanical systems (MEMS), which have been used for sensors and actuators, biomedical devices and wireless communication systems, also require long time and lightweight power sources to be integrated in one small package. The traditional power sources (solar cells, fuel cells, chemical cells) are not compatible to power these devices because of their limitations such as short life span, low energy density and a limited range of temperature at which they can function. For example, one of the main objectives of MEMS technology is a micro size, but due to the low energy density of existing batteries, micro size is not possible, which hinders this important application of MEMS technology. In addition, current batteries are also not well suited for sensors due to their short life span because sensors are often placed in a remote location where periodic recharging or replacement of batteries is highly inconvenient. Furthermore, current micro-power sources are not ideal for devices placed in extreme atmosphere because the chemical reaction rate is influenced by temperature or there may be no sunlight available to power the device.

With their high energy density, long lifetime, and durability in extreme environments, radioisotope-based power sources, which convert radioisotope emissions directly into electrical energy, can overcome these problems [1]. The

energy change "per event" in a radioactive decay is $10^4$ to $10^6$ times greater than that in a chemical reaction, and the energy density of radioactive material is approximately $10^6$ times greater than the energy density of a lithium ion battery [2]. Therefore, radioisotope power sources are very attractive for applications that require a small size, long lifetime and functionality in extreme environments.

The radioisotope sources that are most frequently used are beta emitters with energies << 1 MeV [3]. Beta particles are electrons, and it is their kinetic energy that is converted into electrical energy in betavoltaic cells used in micro power sources. These cells operate on principles similar to those of solar cells [4-5] and differ only in that by using the much more energetic beta rays instead of photons to generate electricity. The energy of the beta particles used for betavoltaics is << 1MeV [3] because it simplifies radiation shielding, packaging and biocompatibility issues. Beta particles with this energy also will not damage the semiconductor causing the properties of the cell to degrade over time. This is the primary reason why the heavier, higher energy alpha particles (helium nuclei) are usually not considered for the energy source [6-7]. Therefore, the discussion will be limited to betavoltaic cells only for this study.

### *1.1 Betavoltaic Cells and their Brief History*

Betavoltaic devices are self-contained power sources that convert high energy beta (β) particles emitted from the decay of a radioactive isotope directly into electrical energy. Beta sources usually have long half-lives, have high energy density and are insensitive to temperature variations. Also, their energy emission is benign, causing very little to no safety hazards. Thus beta sources are very attractive for

micro-power sources to be used for devices requiring low power over a long period of time. The physics behind beta emission, the device structure of betavolaic cells and their operation is discussed in chapter 2.

The electron (beta)-voltaic effect was first reported by Ehrenberg in 1951 when he observed that a selenium photocell was sensitive to electrons when bombarded with an electron beam [9]. However, Paul Rapport was the first person who suggested the use of a *pn* diode for the conversion of beta radiation into electrical energy in 1953 [10]. A selenium photocell (alloy doped silicon) exposed to a high radiation dose of $^{90}$Sr-$^{90}$Y resulted in an overall efficiency of 0.4 %. The following year, similar experiments using silicon and germanium were reported [11-12], but the efficiencies were well below 1%. During the period between the 1960s through the 1990s, numerous laboratories extensively developed and tested betavoltaics, especially Donald W. Douglas laboratories (1968-1974). A device, the Betacell model 400, showed an overall efficiency of approximately 1.7 % by using 77 Ci of promethium-147 (half-life 2.6 years) as a beta emitter. It also found application as a cardiac pacemaker, which was expected to last for 10 years [13-15]. In 1975, the highest overall efficiency of a betavoltaic device was reported with a silicon n/p diode and promethium dioxide and it was only 2.2% [16-17]. From the investigations during that period, not only the overall efficiencies of the devices were poor, researchers also found that beta radiation caused significant damage to the rectifying junction, thus degrading the performance and shortening the lifetime of betavoltaic devices.

Since the 1990s, researchers have investigated different ways to improve the performance of betavoltaic devices. An increase in the surface area of a rectifying junction was introduced in 2003 [18]. The bulk micro-machined silicon *pn* junction was employed to increase the surface-to-volume ratio by 55% and showed a total efficiency of 0.23% with $^{63}Ni$. In order to reduce the radiation damage to the rectifying junction, highly radiation tolerant materials such as silicon carbide (SiC) and indium gallium phosphide (InGaP) were explored. In 2006, a SiC *p-i-n* junction betavoltaic cell was fabricated using chemical vapor deposition on a low resistivity *n*-type 4H-SiC substrate and tested with phosphorus-33 ($^{33}P$). It produced a conversion efficiency of ~4.5% [19]. The device had an output power density of 2.1 $\mu W/cm^2$ and no device degradation effect was observed over 3 months (four half-lives of the source). In the same year, Chandrasekhar investigated a 4H-SiC *pn* structure under the 1 mCi $^{63}Ni$ source and obtained an overall efficiency of ~6%. However, the output power of the device was very low (current density of 16.8 $nA/cm^2$ and open circuit voltage of 0.72 V) [3]. These results showed that the higher output power obtained in [19] was due to the high energy density of the radioactive source $^{33}P$ ($E_{ave}$ = 76.9 KeV) compared to $^{63}Ni$ ($E_{ave}$ = 17.4 KeV) in [5]. Despite these improvements, the basic structure of betavoltaic cells have remained same since their discovery almost 65 years ago, but the maximum efficiencies have only reached approximately 6 %.

*1.2 Motivation*

According to a cited report [20], the output power of a betavoltaic device increases with the increase of the energy gap ($E_g$) of a semiconductor material as shown in figure 1.1. Compared with Si ($E_g$ = 1.12 eV) and 4H-SiC ($E_g$ = 3.21 eV), the

wider energy bandgap of gallium nitride (GaN) with $E_g$ =3.4 eV is a more attractive choice for producing a betavoltaic device.

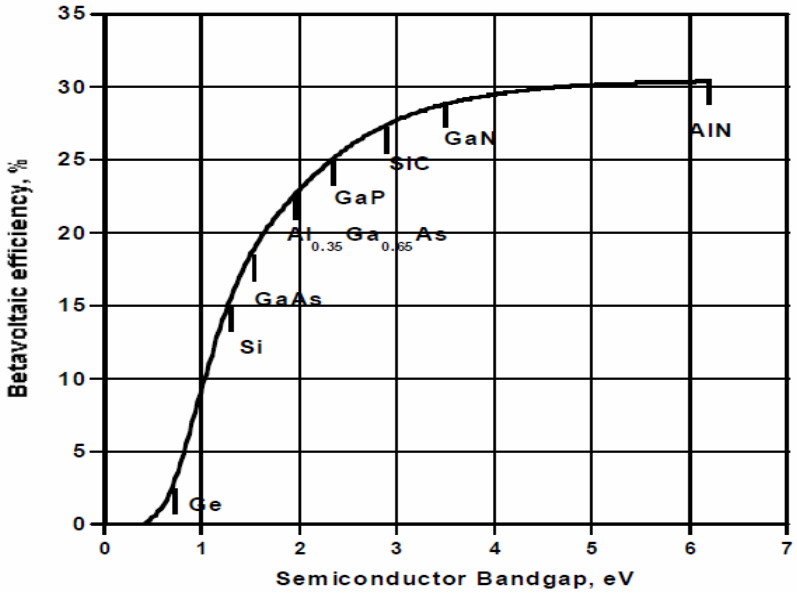


*Figure 1-1 Efficiency as a function of energy band gap*

Wider bandgap semiconductors in general have the advantage of higher radiation resistance, which potentially allows for the use of higher-energy radioisotope sources such as $^{147}$Pm and $^{90}$Sr [21]. Narrow bandgap semiconductors are not suitable for betavoltaic devices because the output power is too low and the cell degrades over time with the beta particles striking it. 4H-SiC is also a good choice since it is an indirect bandgap semiconductor. In indirect bandgap semiconductors, the carriers have more time to diffuse into the depletion region where they are captured by the electric field before they recombine, resulting in a higher output power and increased efficiency. However, GaN has an advantage of flexibility because it can be alloyed with Aluminum (Al) to further increase the energy bandgap, which should allow for more output power and better efficiency.

This enables one to use polarization doping and to more easily use three-dimensional grown structures to increase the efficiency and output power of a betavoltaic device.

There are some challenges associated with GaN that need to be overcome before it can be used successfully for betavoltaic devices. First, GaN films are mostly grown on foreign substrates such as sapphire because, until recently, good quality GaN crystals have not been grown. The structure is a heterostructure – that is, the film and the substrate are different materials. The difference in their lattice parameters is accommodated to some extent by the formation of misfit dislocations, but because it is difficult for them to form and they interact with each other, they cannot accommodate all of the mismatch strain. As a result it is very hard to grow thick GaN layers without forming cracks. A higher resistance GaN layer is needed to increase the width of the depletion region to create a larger volume where the EHPs can be captured by an electric field. However, nominally undoped GaN grown on a sapphire substrate typically shows n-type conductivity with an electron concentration, $n. > 5\times10^{16}$ $cm^{-3}$ due to residual impurities. The hole concentration in *p*-GaN is limited to the range of $1–5 \times10^{17}$ $cm^{-3}$ [22-23]. As a result, the width of the depletion region of the GaN p-n junction is too narrow to effectively collect radiation-generated electron hole pairs (EHPs) to provide sufficient current for the battery output.

To improve the performance of 2-dimensional GaN betavoltaic batteries, it is necessary to investigate ways to maximize the width of the depletion region to collect the maximum number of the generated EHPs. Zaijun Chen *et. al.* used the process of Fe doping, compensation for the unintentionally doped GaN layer, to increase the width of the depletion region. They were able to increase its width to 900 nm on a p-i-

n diode and obtained an open circuit voltage of 1.64V by using $^{63}$Ni as a beta source (activity of 0.5mCi) [24]. Zaijun and his group also investigated the p-n diode junction betavoltaic battery on GaN, but only measured a maximum open circuit voltage of 35 mV [25]. With the exception to the previously mentioned studies, there have been very few experimental reports on GaN *p-i-n* junction betavoltaic micro-batteries. To the best of my knowledge, there are no current reports on AlGaN betavoltaic devices.

In this thesis, GaN *p-i-n* junction betavoltaic devices are investigated. Their behavior for a beta source is simulated using an electron beam in a scanning electron microscope (SEM) with various energies. This work includes the development of *p-i-n* devices for betavoltaic micro-batteries from their design, fabrication, and characterization to enhancing their performance.

### *1.3 Contributions*

1. Developed the process for fabricating devices for betavoltaic microbatteries on GaN.
2. Developed the protocol for testing and evaluating their performance as betavoltaic microbatteries. A 400 μm x 400 μm device showed an output power of 640 nW with an overall efficiency of 4% when evaluated for $^{63}$Ni beta source.
3. Identified parameters for optimized performance on GaN.
4. AlGaN betavoltaic devices are being fabricated and characterized for the first time as a work in progress.
5. Publications:

a. "GaN based p-i-n devices for Betavoltaic Microbatteries" Electronic Materials Conference (EMC) Columbus, Ohio, June 25th 2015.

b. Solid State Electronics Journal paper in preparation.

*1.4 Overview of Chapters*

In Chapter 1, an introduction to betavoltaic microbatterries, their brief history and current status of the related research and developments are mentioned. Chapter 2 covers the physics of betavoltaic cells from device structure to its operation. The overview of beta decay, their energy spectrum and properties of the beta sources used in this study are also mentioned.

Chapter 3 covers the experimental section of this work. This chapter is focused on the design, fabrication and characterization of these devices. Chapter 4 provides an overview of all the equipment used in this study. Chapter 5 is results and discussion. In this chapter, all the results are analyzed and discussed in details.

In chapter 6, a summary of the thesis is presented. The future work is discussed along with the work in progress.

# Chapter 2. Betavoltaic Cell Physics

## *2.1 Beta Particles and their Energy Spectrum:*

Beta (β) particles are high energy electrons emitted from an unstable nucleus with an established spectrum of kinetic energies. Nuclei are said to be unstable with respect to β decay when there is an "out of balance" between the numbers of neutrons and protons [26]. In a very qualitative way, beta decay converts a neutron into a proton (or vice versa) inside the nucleus of an atom. Two particles are created during the beta decay process, beta particle (electron or a positron) and a chargeless particle (neutrino or an antineutrino) which has a zero to negligible rest mass [27]. The process in which a neutron in the nucleus of an unstable atom is converted into a proton is called the $\beta^-$ (beta minus) decay. During this conversion an electron and an antineutrino are ejected by the nucleus and its reaction [27] is given by:

$$ {}^{A}_{Z}P \rightarrow [{}^{A}_{Z+1}D]^{+} + {}^{0}_{-1}e + \overline{ve} \qquad (1) $$

$$ n \rightarrow p + e^{-} + v^{-} \qquad (2) $$

Where $^{A}P$ is the parent nuclei, $^{A}D$ is the daughter nuclei, Z is the number of protons, $e^-$ and $\overline{ve}$ represent the ejected electron and anti-neutrino, respectively. The above reaction shows that a neutron rich radioactive nuclide decays by changing a neutron in the parent (P) nucleus into a proton. The daughter atom denoted by $[{}^{A}_{Z+1}D]^{+}$ gains a proton, initially lacks one orbital electron, and thus it is a singly charged positive ion [27].

The beta decay energy is obtained from the Q-value of the decay reaction. For $\beta^-$, the energy of emission [27] is given by:

$$Q_{\beta}^{-}/c^2 = M({}_{Z}^{A}P) - M({}_{Z+1}^{A}D) \quad (3)$$

Where M is the atomic mass of the nuclide involved and c is the speed of light. For $\beta^-$ decay to occur spontaneously, $Q_{\beta}^{-}$ must be positive or, equivalently, the mass of the parent atom must exceed the mass of a daughter atom, i.e $M({}_{Z}^{A}P) > M({}_{Z+1}^{A}D)$ [27]. For $Q_{\beta}^{-}$, typical values are ~ 0.5 to 2.0 MeV [26].

The $\beta^+$ (beta plus) decay, also known as positron emission, is the exact opposite of a $\beta^-$ decay process. In this process, a proton in the nucleus of an unstable atom is converted into a neutron [26]. This process yields an emission of a positron ($e^+$) and a particle, neutrino ($\nu$). Its reaction [27] is given by:

$${}_{Z}^{A}P \rightarrow [{}_{Z-1}^{A}D]^{-} + {}_{+1}^{0}e + \nu e \quad (4)$$

$$p \rightarrow n + e^{+} + \nu \quad (5)$$

$Q_B^+$ is the emission energy of the positron decay and is given by:

$$Q_{\beta}^{+}/c^2 = M({}_{Z}^{A}P) - M({}_{Z+1}^{A}D) - 2m_e \quad (6)$$

M is the atomic mass of the nuclide involved and $m_e$ is the electron mass. For $Q_B^+$, typical values are ~ 2 to 4 MeV [26].

The electron capture reaction competes with, or substitutes the positron emission.

$${}_{Z}^{A}P \rightarrow [{}_{Z-1}^{A}D]^{*} + \nu_e \quad (7)$$

$$p + {}_{+1}^{0}e \rightarrow n + \nu \quad (8)$$

Where $Q_{EC}$ is the energy of the electron capture process and is given [27] by:

$$Q_{EC}^{-}/c^2 = M({}_{Z}^{A}P) - M({}_{Z-1}^{A}D) \quad (9)$$

Typical values of $Q_{EC}$ range from ~ 0.2 - 2.0 MeV [26].

Beta particles are always observed to possess a continuous spectrum of energies extending from essentially zero up to a maximum [28]. It is important to know what the energy of the electron is because it determines how far the electron penetrates into the semiconductor, and to what extent it creates point defects such as vacancies and interstitials in the lattice. Figure 2.1 shows the energy spectrum of the beta minus and the beta plus decay processes [29].

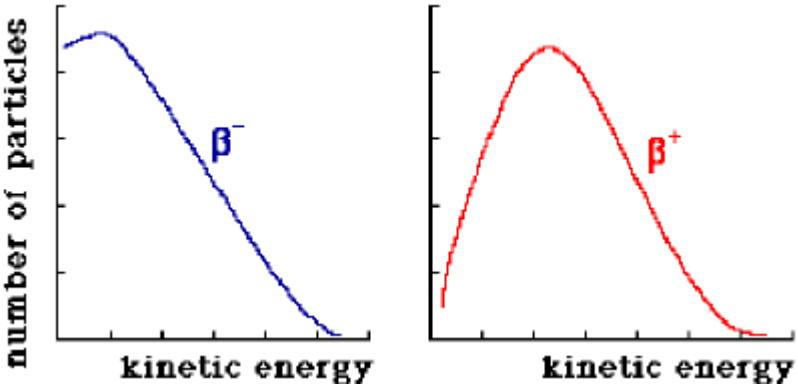


*Figure 2-1 Energy spectrum for B- and B+ decay*

Several hundred beta sources are known; some are naturally occurring and others are artificially made in the lab [26]. The energies of the beta sources range from a few KeV to more than 15 MeV and their half-lives from about a second to hundreds of years [31]. Selection of a beta source for a power source applications depends on parameters such as its half-life, cost, reliability, and average energy emission. In this work, we will focus on Tritium and Nickel-63 as beta sources for our power source because of their long half-lives (>12 years) and low energy emission that won't damage the lattice, yet significant output power.

### 2.1.1 Tritium ($^{3}H$)

$^{3}H$ is a radioactive isotope of hydrogen that contains one proton and two neutrons. $^{3}H$ is a pure *(naturally found)* beta emitter which has a half-life of 12.5 years, an average energy of 5.7 keV and a maximum energy of 18.6 keV. $^{3}H$ can be used in a gas phase and it can be combined with a metal to form a metal hydride or incorporated into a solid organic metal such as a plastic. The mean penetration depth of $^{3}H$ in GaN is ~ 0.3 μm [36] and its typical activity is ~ 2.6 Ci/mmol [35]

### 2.1.2 Nickel-63 ($^{63}Ni$)

$^{63}Ni$ is not a pure beta emitter; it is prepared by neutron irradiation of a target containing nickel-62 as a base isotope. It has a half-life of 100 years, average beta energy of 17.4 keV and a maximum energy of 65.9 keV. The mean penetration range of $^{63}Ni$ in GaN is ~ 1.80 μm [36]. $^{63}Ni$ can be evaporated on the films just like other metal as well as be deposited using an electrodeless technique with an aqueous solution of nickel salt and hypophosphite [37].

## *2.2 Betavoltaic Cell Device Structure*

A betavoltaic cell has two components as shown in figure 2.2. One is the radioactive source, and the other is the semiconductor diode with its *p-n* or metal-semiconductor junction. Radioactive sources are mentioned in the previous section. In this section, the structure of a semiconductor junction is discussed.

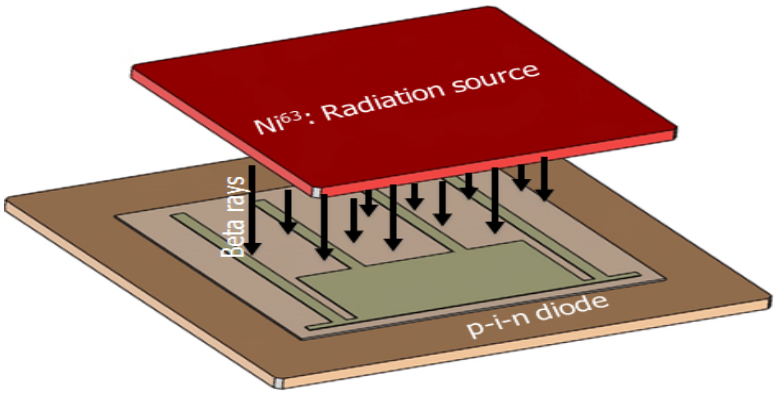


*Figure 2-2. Betavoltaic microbattery*

The most commonly used betavoltaic devices are made by creating either a *pn* or a *p-i-n* junction in the semiconductor. The *i* (intrinsic) layer is added to the *pn* junction to increase the width of the depletion region. A wider depletion region enables the capture of more of the carriers generated by the collision of the beta particle with the lattice, thus increasing the output power and efficiency of the device. For this work, we will focus on *p-i-n* rectifying junctions. Figure 2.3 shows a cross-sectional schematic of a typical *p-i-n* junction betavoltaic cell.

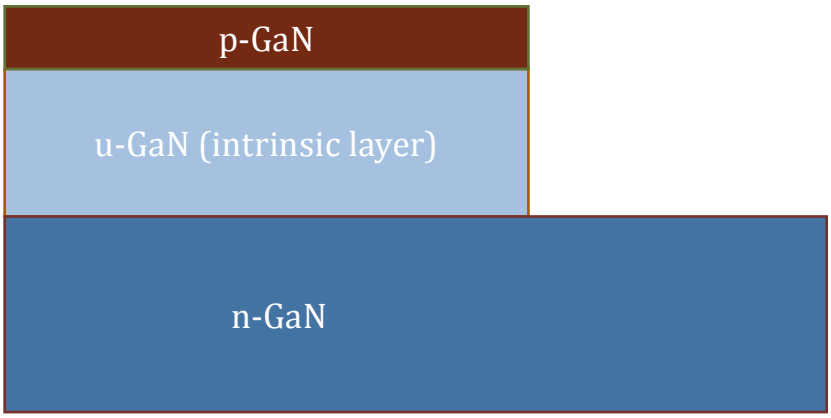


*Figure 2-3 cross-sectional schematic of a typical p-i-n junction betavoltaic cell.*

The layer that is illuminated first is the top p-layer. It is usually made very thin so that most of the beta particles can penetrate to it and generate the maximum

number of electron hole pairs (EHPs) in the depletion region where they are quickly separated and collected by the electric field. Because the p-layer is made thin, it must be heavily doped so that it will not be completely ionized by the depletion layer destroying its ability to act as an effective *pn* junction; this phenomenon is called punch through. The base layer (n-layer) is also heavily doped because this reduces the on-resistance, $R_{on}$. The middle *i*-layer is not intrinsic as suggested by the name. The intrinsic case – doping in the range of $<10^{10}$ - would not only be difficult to attain, but extremely low doping would cause the device to have a large $R_{on}$ [31]. Hence, the so called intrinsic layer is actually an $n^-$ (n minus) layer with a doping concentration of a few orders of magnitude lower than the $n^+$ layer. The low doping creates a wider depletion region where virtually all of the EHPs generated in it are captured by its electric field. It also increases the probability that the carriers created outside of the depletion layer, but close to it, will be captured by the E-field in the depletion region by diffusing to it before recombining. The lower doping in the intrinsic region also ensures higher minority carrier lifetime and higher diffusion coefficients, which in turn increase the carrier diffusion length. In GaN *p-i-n* structures, the intrinsic layer with a doping concentration less than $10^{16}$ $cm^{-3}$ has not been successfully grown yet. Due to this reason, the depletion region width cannot exceed ~ 500 nm. Thus, the *i*-layer should not be grown much thicker than 500 nm because the carriers created in it that are too far from the depletion region will not add anything to the beta-current, but will increase $R_{on}$.

*2.3 Betavoltaic Cell Device Operation*

In a betavoltaic cell, beta particles incident upon a semiconductor generate EHPs when they collide with a lattice. This is analogous to how a photovoltaic device operates: photons with energies higher than the band-gap energy of the cell get absorbed and generate EHPs. An absorbed photon usually generates only one EHP. On the other hand, beta particles have much higher energies and a single incident beta particle can generate many EHPs. As beta particles penetrate into the semiconductor, they undergo many inelastic collisions. A part of their energy is used to excite electrons from the valence band into the conduction band creating EHPs, and the rest of the energy is lost as heat through phonon interactions in the semiconductor [33]. Essentially all of the EHPs generated in the depletion region contribute to the $\beta$-current density, $J_\beta$, because they are swept out by the electric field in it. Some of the EHPs generated near the depletion region diffuse into it before they recombine and are swept out by the E-field in the same manner. They are the $\beta$-induced electrons in the *p*-material and the $\beta$-induced holes in the *n*-material. Only EHPs generated within a diffusion length from the depletion region or inside the depletion region are collected and produce current.

The average distance the minority carrier can diffuse before it recombines is the minority carrier diffusion length ($L_n$ or $L_p$), which depends on the average time it takes to recombine, the minority carrier lifetime ($\tau_n$ or $\tau_p$), the rate at which it diffuses, and the minority carrier diffusion coefficient ($D_n$ or $D_p$). The relationship is given [34] by:

$$L = \sqrt{D\tau} \qquad (10)$$

$$\frac{D}{\mu} = \frac{kT}{q} \qquad (11)$$

Where μ is the carrier mobility.

When there are no external effects on the semiconductor junction (betavoltaic cell) such as an applied voltage, light, or $\beta$-particles, no net current flows through the junction because there is a diffusion current density that is equal to the drift current density but flows in the opposite direction. This is known as the steady state condition. Diffusion current originates due to the concentration gradient between the *n* and *p* materials. A *p*-layer contains a large concentration of holes wanting to diffuse into the *n*-material where there are virtually no holes. The same thing is true for electrons on the *n*-side wanting to diffuse into the *p*-material. Holes that diffuse into the n-material leave behind negatively charged ions, and electrons that diffuse into the p-material leave behind positively charged ions. These charges (positive and negative ions) are fixed and the region containing these fixed charges is called the space charge region or the depletion region. These fixed charges create the electric field in the depletion region, which points from the n-side to the p-side. This electric field works against the diffusion of carriers, wants to keep holes in the p-side and electrons in the n-side. Due to this electric field, drift current arises which drifts the holes in the n-material back to p-side and electrons from the p-material back to n-side. The electrons created thermally in the *p*-material and the holes created thermally in the *n*-material behave in the same way, and they create a current density, $-J_s$, often called the reverse saturation current density. It is negative because the holes are drifting towards the *p*-side and electrons are drifting towards the *n*-side.

At steady state, no net current flows through the junction and the Fermi energy levels of n and p type materials line up causing band bending, as shown in figure 2.4. The band bending creates a potential barrier at the junction. The potential barrier is created by electrons flowing over to the *p*-side and ionizing the acceptors with negative charge, while leaving positively charged donors on the *n*-side. The Fermi energy levels: $E_{Fn}$, is a measure of concentration of electrons in the conduction band and $E_{Fp}$ is a measure of concentration of holes in the valance band. In n-type material, $E_{Fn}$ lies closer to the conduction band and the thermal-equilibrium electron concentration is given by:

$$n = ni * \exp\left[\frac{E_F - E_{Fi}}{KT}\right] \quad (12a)$$

where $n_i$ and $E_{Fi}$ are the carrier concentration (electrons in the conduction and holes in the valence band) and Fermi energy level of an intrinsic (undoped) material, respectively. $E_{Fi}$ lies very near the middle of the energy gap in an intrinsic material.

In *p*-type material, $E_{Fp}$ lies closer to the valence band and the hole concentration is given by:

$$p = ni * \exp\left[\frac{-(E_F - E_{Fi})}{KT}\right] \quad (12b)$$

If we make the assumption that $n = N_d$ in the *n*-type material, and $n = N_a$ in the *p*-type material, where $N_d$ and $N_a$ are, respectively, the donor and acceptor concentrations – this is a good assumption for shallow dopants at room temperature – then the built-in potential barrier, $V_o$, is found from the equation 13:

$$qVo = E_{Fn} - E_{Fp} = kTln\left(\frac{N_A N_D}{ni^2}\right) \quad (13)$$

The built-in potential barrier to the diffusion current can be altered by applying a voltage; a forward bias will lower the barrier, while a reverse bias will

raise it. Since the probability that a carrier can diffuse over the potential barrier depends exponentially on the height of the barrier, the diffusion current can be written as

$$J_{diff} = Js * \exp\left(\frac{qV}{kT}\right) \quad (14)$$

Where k is Boltzmann's constant, V is the applied voltage (note that a reverse voltage is negative) and T is the temperature. The drift current is not affected by the applied voltage so the total current density when the diode is not exposed to light or $\beta$-particles is,

$$J = Js * [\exp\left(\frac{qV}{kT}\right) - 1)] \quad (15a)$$

In a betavoltaic device, when the diode is exposed to $\beta$-particles, the current density is described by the equation

$$J = Js * [\exp\left(\frac{qV}{kT}\right) - 1)] - J\beta \quad (15b)$$

If the diode is not connected to an external load, charge will build up on either side of the junction with the *p*-side becoming positively charged by the injection of the $\beta$-excited holes, and the *n*-side becoming negatively charged by the injection of the $\beta$-excited electrons. This charge creates a positive voltage, which will lower the barrier height, which will increase the diffusion current. A steady state will be reached when there is no net current flow because the diffusion and drift currents are now equal but opposite. One can easily show the voltage across the junction when this occurs, the open circuit voltage, $V_{oc}$ by:

$$V_{oc} = \left(\frac{kT}{q}\right) * \ln\left[1 + \left(\frac{J_\beta}{Js}\right)\right] \quad (16)$$

It can be seen from the above equation that $V_{oc}$ will be larger when $J_s$ is smaller. $J_s$ is smaller in wider band gap semiconductors because fewer thermal electrons and holes can be created because they are formed by electrons jumping over the energy gap, $E_G$. It can, in fact, be shown that $J_s$ is proportional to $e^{-E_{G/kT}}$. Due to this reason, wider band gap semiconductors always have higher $V_{oc}$ and it goes up as the energy gap of a material is increased. Note from the discussion above that $V_{oc}$ cannot exceed $V_o$, because when it is equal to it, there will be no potential barrier to affect the current flow. Since the Fermi energies in the *p* and *n* material are further apart for the same doping levels in wider band gap semiconductors, $V_{oc}$ will also be larger.

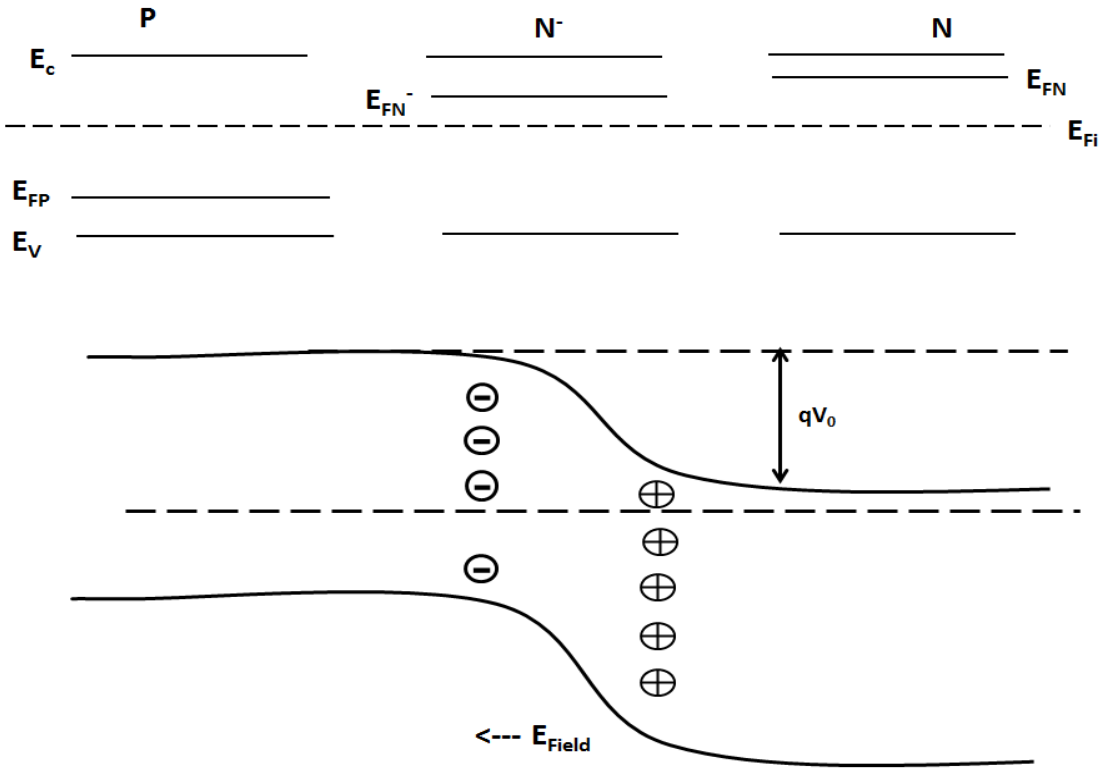

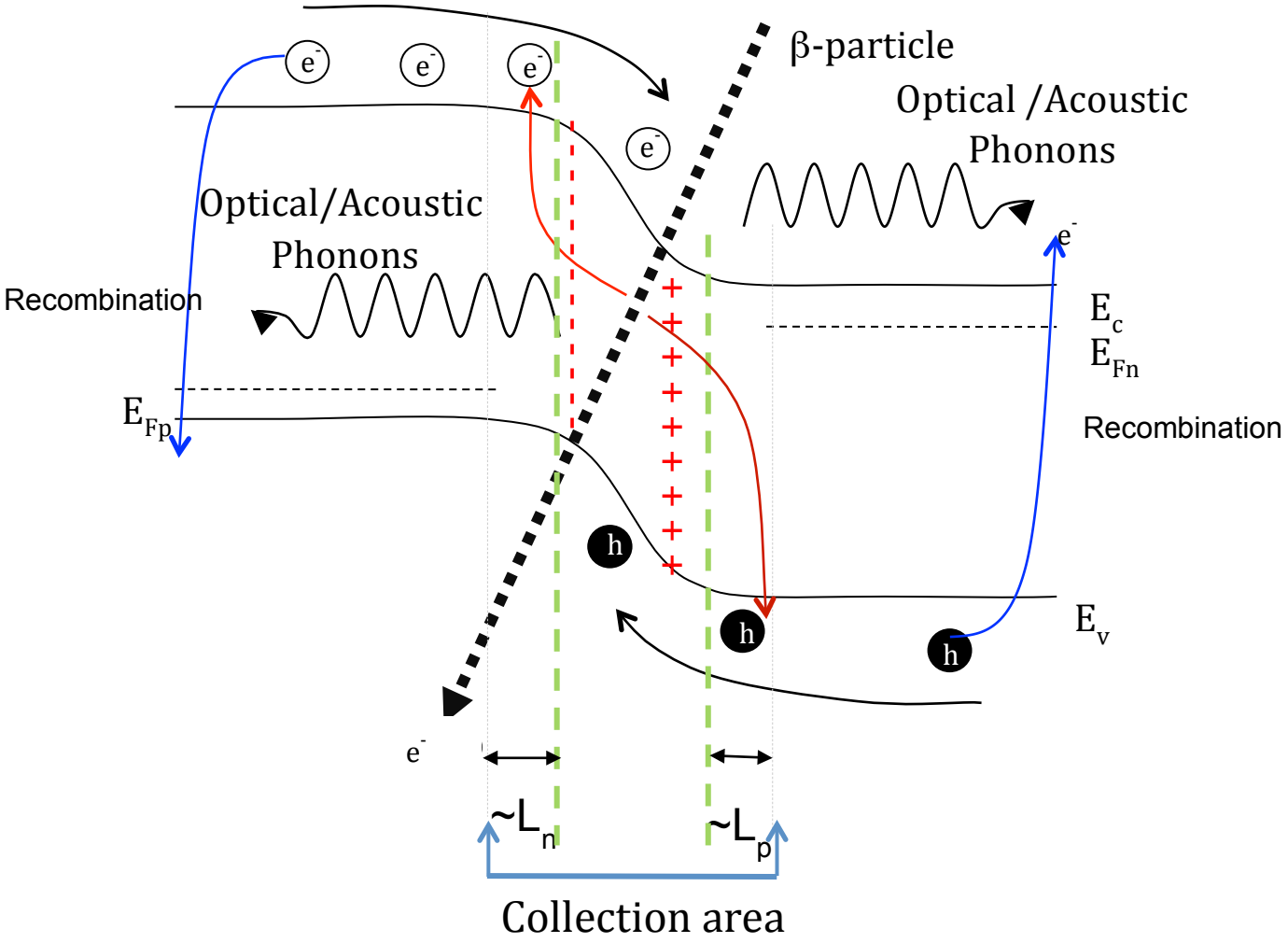


*Figure 2-4 device operation (top) under equilibrium when Vbias = 0 and (bottom) under beta illumination*

When the diode is shorted so that no voltage is applied across the junction; there is no diffusion current to offset Jβ, so now the current density is -Jβ. This is also called the short circuit current density, Jsc.

For an abrupt junction where both sides of the junction are uniformly doped, the electric field plotted as a function of position, is a triangle with the maximum value, $E_o$, at the interface being equal to

$$E\max = \frac{-qN_d x_n}{\varepsilon} = \frac{-qN_a x_p}{\varepsilon} \qquad (17)$$

Where $x_p$ and $x_n$ are the width of the depletion region (W) in the *p*- and *n*-type material, respectively and ε is the electrical permittivity of the semiconductor.

$$x_n = \sqrt{\frac{2\varepsilon}{q} Vo[\frac{N_a}{N_d}] * \frac{1}{N_a+N_d}} \qquad (18)$$

$$x_p = \sqrt{\frac{2\varepsilon}{q} Vo[\frac{N_d}{N_a}] * \frac{1}{N_a+N_d}} \qquad (19)$$

$$W = x_n + x_p = \sqrt{\frac{2\varepsilon Vo}{q} * \frac{N_a+N_d}{N_a N_d}} \qquad (20)$$

The area of the triangle is equal to $\frac{1}{2}E_oW$, which is equal to the voltage across the junction, $V_o$ - V.

$$Vo - V = \frac{qN_aN_dW}{\varepsilon(N_a + N_d)} \qquad (21)$$

Under beta irradiation, the generation of EHPs does not significantly increase the majority carrier concentration. However, the minority carrier concentration is significantly increased and hence, the diffusion current dominates due to the concentration gradient developed in the quasi-neutral region. As noted above, the flow of generated minority carriers essentially defines the direction of the beta-induced current density flowing from the *n*-terminal to *p*-terminal. Collection of all the negative charges on the *n* side and positive charges on the *p* side creates a beta-induced forward bias to the betavoltaic cell. As a result of this forward bias in the presence of an external load, diode current begins to flow in the opposite direction to the beta-generated current and is typically referred to as diode dark current, $J_{dark}$. It is important to minimize the dark current as it reduces the beta-generated current.

### 2.3.1 Characteristics of Betavoltaic Cells

The current density given by eq. 15a is for an ideal diode. In a real diode there are point defects in the depletion region called traps that often lie near the middle of the energy gap that can trap some of the carriers as they cross the depletion region. Trap states decrease the current density and are accounted phomenonlogically by inserting a number, *n*, called the ideality factor, into the exponent, as illustrated in eq. 22:

$$J = J_s\left(e^{\frac{qv}{nkT}} - 1\right) \qquad (22)$$

When the traps have a dominant effect, the value of $n \approx 2$, and when their effects are small, $n \approx 1$ are observed [*12*].

$J_s$ in the ideal diode is quite small, but it can be increased by crystalline line defects such as dislocations lying in the depletion region. They can supply pathways for diffusing carriers through the depletion region that have energy barriers that are smaller than the contact potential so more carriers can diffuse across the junction. This additional current is called the leakage current [*12*].

The performance of a betavotaic device is analyzed with or without beta illumination. For a device under beta illumination, eq. 22 for the current density is modified by $J_\beta$ so,

$$J = J_s\left(e^{\frac{qv}{knT}} - 1\right) - J_\beta \qquad (23)$$

$V_{oc}$ increases with the increase in the value of $J_s$, as shown in eq. 24.

$$V_{oc} = \frac{nkT}{q} ln\left(1 + \left(\frac{J_\beta}{J_s}\right)\right) \qquad (24)$$

As noted in the discussion above, Js decreases exponentially with the energy gap, so it is very small for the larger band gap semiconductors, and is therefore more sensitive to the increases caused by defects. It is therefore even more important for the wider band gap semiconductors to have very high quality *pn* junctions.

Since β-generated current density is negative, the I-V curve drops down into the 4$^{th}$ quadrant, which indicates the device is generating, as opposed to consuming, power. The current-voltage (I-V) characteristics of a betavoltaic device under beta irradiation (green curve) and under no irradiation (orange curve) are represented in figure 2.5.

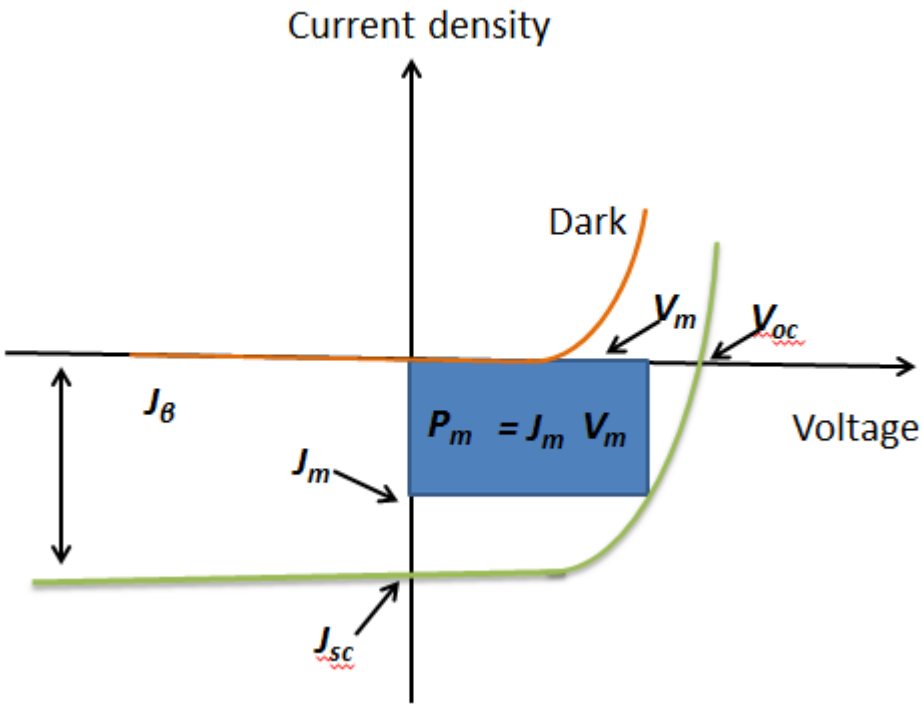


*Figure 2-5 IV characteristics of a device in the dark and under beta illumination*

When V = 0, the current is equal to the negative of the short circuit current, $J_{sc}$, which is the same as $J_\beta$, and it is equal to $V_{oc}$ when no current is flowing

We want to maximize this but we have practically no control over how much of the beta particle's energy is converted into EHPs. This is dictated by the physics and it is ~ 35% for the wider band gap semiconductors [33]. However, we do have control over the number of electrons and holes that can be captured before they recombine. The efficient way to do this is to create EHPs in the depletion region where the probability of capture is almost 100% because there is an electric field that can sweep out the carriers. A width of the depletion region is given by eq. 20.

The average penetration depth of $^{63}$Ni and Tritium are ~1.80 μm and ~ 0.3 μm, respectively [36]. We want the p-layer to be much thinner than the penetration depths because the β-electrons created in it probably won't reach the junction if the p-layer is thicker than the penetration depth. However, we want the depletion region width to be larger than the penetration depth so EHPs can be efficiently created and captured there. In order to deliver real power to the load, the betavoltaic cell does not operate in open circuit voltage or short circuit configurations. Instead it operates under the illuminated IV characteristics between the two extremes as shown in figure 2.5. The maximum power from the betavoltaic cell is obtained when the resistance of the load is selected such that it allows the current-voltage product to be maximized. The point at which this output power is maximized is called the maximum power point, $P_m$ and can be expressed as:

$$P_m = J_m V_m \tag{25}$$

Where $J_m$ and $V_m$ are the peak current density and peak voltage points, respectively. The efficiency of a betavoltaic device ($\eta$) describes its ability to efficiently convert incident beta electrons into output electrical power. It can be

described as the amount of maximum power density delivered ($P_m$) as a fraction of the incident beta power density from the radioactive source and can be expressed as:

$$\eta = \mathrm{FF}\frac{V_{oc}*J_{sc}}{E_\beta*J_\beta} \qquad (26)$$

Where $E_\beta$ is the mean incident energy of beta radiation and $J_\beta$ is the incident flux of β-particles. Claude Klein showed empirically that when a beta particle creates an EHP, the average energy it gives up is $2.8\,E_g + 0.5\,eV$, with $1.8\,E_g$ of that energy is lost to optical phonons and 0.5 eV is lost to acoustic phonons. This accounts for 65% of the total beta energy not used in creating EHPs, which caps the betavoltaic conversion efficiency to only 35% [33]. This means that the betavoltaic device cannot be more than 35% efficient.

Figure 2.6 shows the equivalent circuit model of a betavoltaic cell that takes into account the series resistance ($R_s$) and shunt resistance ($R_{sh}$).

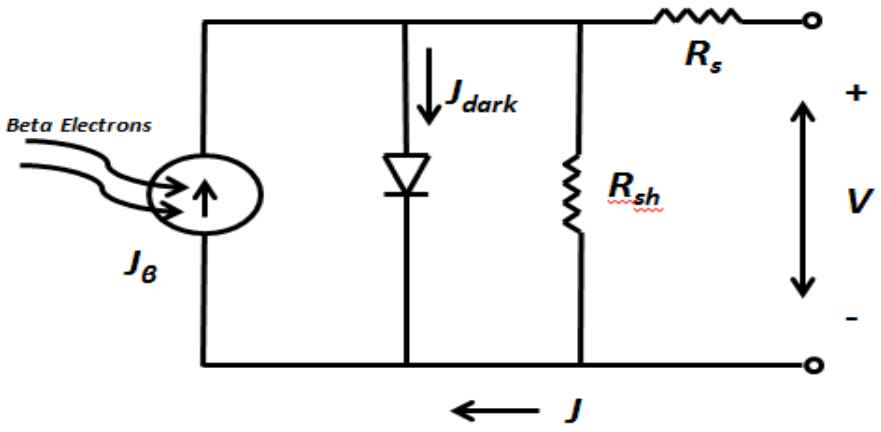


*Figure 2-6 equivalent circuit taking into account series and shunt resistances*

The current density taking into account the influence of series resistance ($R_s$) and shunt resistance ($R_{sh}$) is given by equation 27:

$$J = J_{\beta} - Js\ (\exp\left[\frac{V+J_{RS}}{\frac{nKt}{q}}\right] - \frac{V+J_{Rs}}{R_{sh}}) \qquad (27)$$

$R_s$ and $R_{sh}$ to some extent are dictated by the thickness of the *i*-layer. If it is too thin, the depletion layer will punch through and the resistance will be negligible. If it is too thick, it will increase the resistance, since it has a much lower doping level. A good estimate of the ideal thickness is the thickness of the depletion layer plus the minority carriers' diffusion length.

# Chapter 3. Fabrication and Characterization of Devices

In this work, p-i-n devices for betavoltaic microbatteries were fabricated on GaN structure grown epitaxially by metal organic chemical vapor deposition (MOCVD). Devices were fabricated using the standard photolithography, plasma etching, and metallization techniques. The devices were characterized using current-voltage (I-V) and the photo-response behavior. In order to emulate their behavior for a betavoltaic microbattery, devices were tested under an electron beam at various energies. Electron beam induced current (EBIC) measurements were performed to evaluate the different regions of the devices.

The GaN sample was grown on a 2-inch sapphire ($Al_2O_3$) substrate by our collaborator at SUNY Albany using a Veeco D180 MOCVD reactor. The device structures were grown on a sapphire substrate because it is a cheaper alternative to growing it on the bulk GaN substrate. The lattice mismatch between the sapphire substrate and GaN film is 16%, which causes large stresses and strains in the film. These stresses and strains are negated by growing a buffer layer deposited at a low temperature on top of the substrate before growing the active GaN films. The film structure of this sample is shown in figure 3.1.


*Figure 3-1 Film structure of the GaN sample*

The unintentionally doped GaN was doped with magnesium to achieve the p-type carrier concentration of 4 x $10^{17}$ $cm^{-3}$ and with silicon for n-type carrier concentration of 3 x $10^{18}$ $cm^{-3}$. The p-type dopants were activated using a rapid thermal anneal at 700 ºC for 60 s to remove the H atoms that were weakly bonded to the Mg atoms. The carrier concentration of intrinsic GaN layer is $1x10^{16}$ $cm^{-3}$ and it is 1 μm thick. A buffer layer (n-GaN template of 4 μm) was grown on top of a sapphire substrate in order to relax the film from stresses and strains in order to avoid cracking.

A dicing saw was used to dice the sample into 1 cm x 1 cm pieces. The sample was diced to fit it into standard 40 pin Dual Inline Packages (DIP) available at our laboratory. After dicing, the sample was transferred to a class 100 cleanroom located at the Army Research Laboratory (Adelphi, MD) for device fabrication.

Initially, I degreased the sample to remove organic and ionic contaminants. Our standard degreasing process consists of three sequential two-minute acetone baths that includes sonication. After the final acetone bath, the sample was rinsed with methanol to remove any acetone residue and then blown dry with ultra-high purity (UHP) $N_2$ gas. The degreasing process outlined above was performed in a solvent fume hood.

A diced piece from each sample was fabricated using a photomask set shown in figure 3.2.

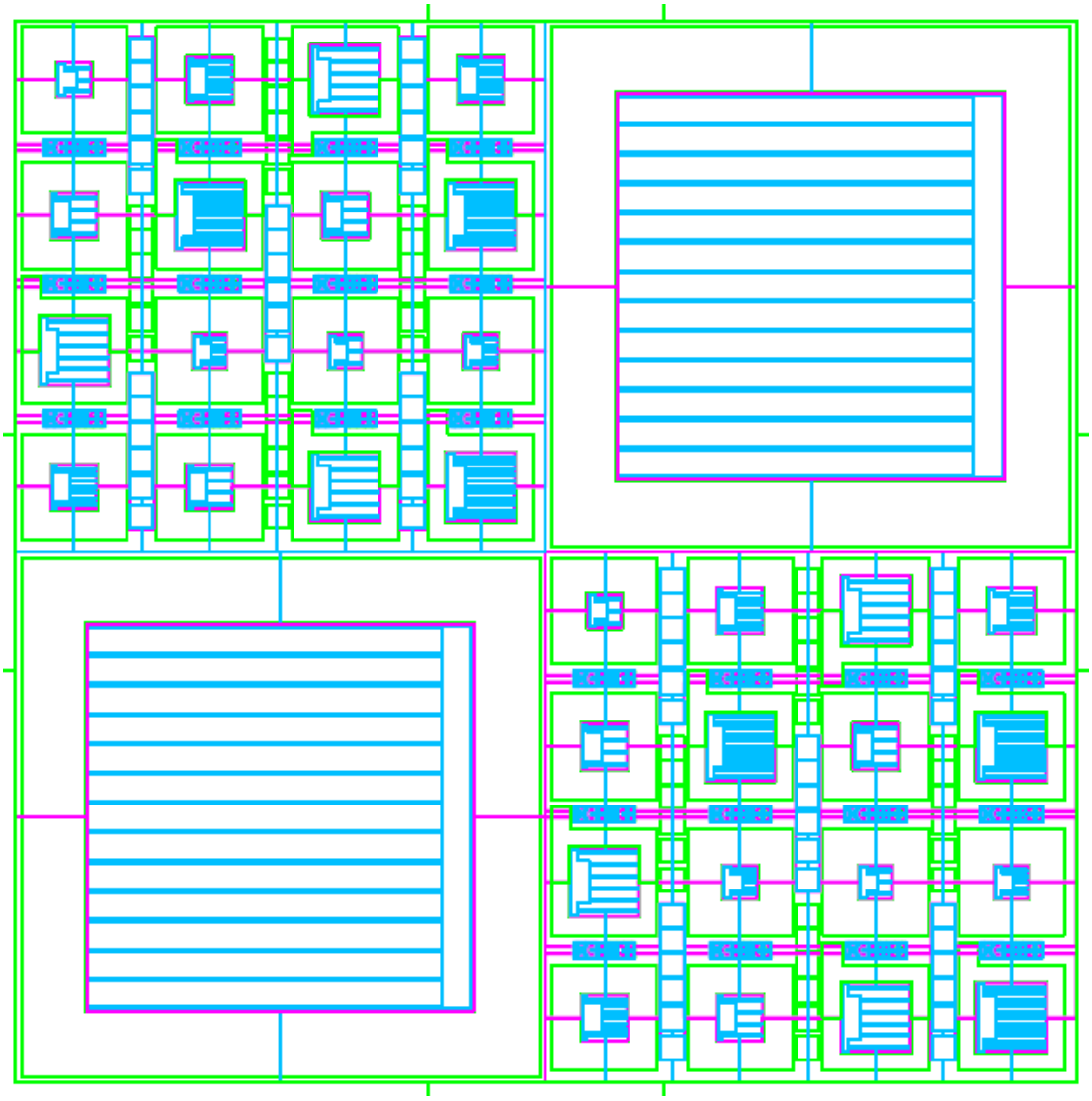

*Figure 3-2 photomask used for fabrication of devices*

The photomask was designed for four operations: mesa pattern layer, n-contact pattern layer, p-contact pattern layer and wire bond metal layer. It contains a total of 34 devices with 4 different sizes (300 x 300 µm, 4000 x 400 µm, 600 x 600 µm and 3.3mm x 3.3 mm. The devices with different sizes and geometries were designed to determine which devices have a better performance for a betavoltaic device.

The sample was fabricated in the cleanroom. The fabrication steps are discussed in details below:

### 1. Mesa Pattern

First, a mesa pattern was formed on the sample using the mesa layer photomask. This was done using the negative (image reversal) process with the AZ5214E photoresist. Initially, AZ-5214E was applied to the sample and spun at 2000 RPM for 40 s to get a uniform coating of the resist. Next, the samples were baked on a hot plate at 110°C for 60 seconds to drive off the solvents. After that, the samples were aligned and exposed for 4.2 s using the mask aligner (MA-6) to transfer the pattern from the mask to the sample. Next, the samples were baked at 120ºC for 30 s before flood exposing it for 8 s using the mask aligner. Samples were developed (75 s) in AZ 300 MIF and the metroline asher was used to descum the structures for 5 min to remove any residual photoresist. Finally, the samples were loaded into the CHA metal evaporation system and Cr/Ni (25/800nm) were evaporated onto the samples to be used as an etch mask.

### 2. Etch

The next step was to etch the mesa to expose the n-type GaN layer for ohmic contact deposition. The inductively coupled plasma (ICP) etch system was used to etch the samples using $BCl_3/Cl_2/Ar$ plasma chemistry. The Cr/Ni (25/800 nm) etch mask was used to prevent the mesa structures from being etched as shown in figure 3.3. The selectivity of Ni to GaN is 15:1 in the ICP etch. The GaN etch rate was determined to be ~300 nm/minute. The sample was etched ~1.2 μm and the etch thickness was confirmed using the stylus profilometer.

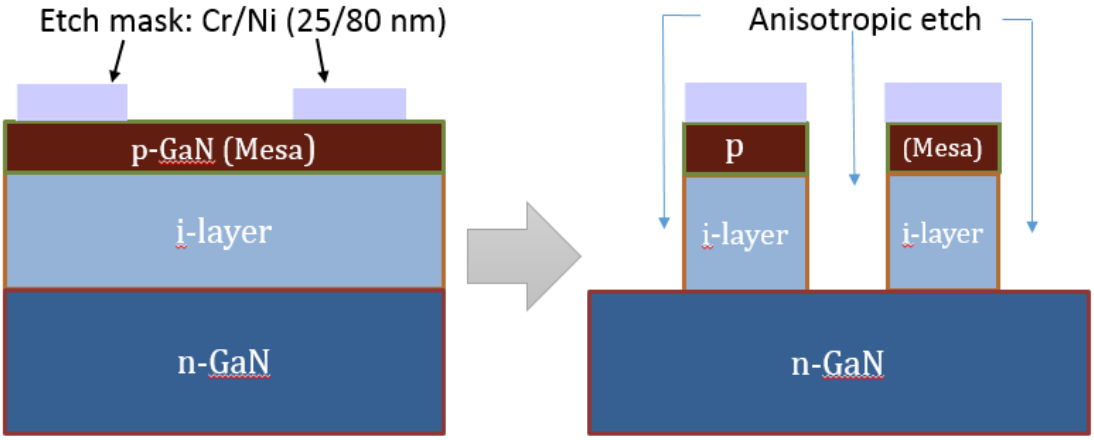


*Figure 3-3 ICP etch flow diagram*

The Cr/Ni metal stack was removed from the sample using the chrome etchant. The wafer was placed in the chrome etchant chemical for ~2 minutes to remove all the metal. Next, sample was degreased with acetone/methanol and blown dry with ultra-high purity (UHP) $N_2$ gas to prepare it for n-type ohmic contact deposition.

### 2. N-type Ohmic Contact Deposition

To deposit n-type ohmic contacts, the sample was patterned using the positive photolithography process with AZ5214E. Initially, AZ-5214E was applied to the sample and spun at 2000 RPM for 40 s to obtain a uniform coating of the resist on the sample. Next, the sample was baked on a hot plate at 110 °C for 60 s. After that, the sample was aligned and exposed for 8 s using the mask aligner (MA-6) to transfer the pattern from the n-type ohmic mask layer to the sample. The sample was developed in AZ 300 MIF for 75 s and the metroline asher was used to descum the sample for 5 min to remove any residual photoresist.

Next, the sample was wet etched in HCl for 60 s to remove the thin oxide layer created by exposing the etched sample to the atmosphere before immediately

loading it into the CHA-e-beam evaporator for metal deposition. The CHA metal evaporation system was pumped to a base pressure of $2x10^{-6}$ and a Ti/Al/Ni/Au (250/2200/600/500 Å) structure was deposited. After metal deposition, the lift off technique (acetone ultrasonic bath) was used to remove the metal from the mesas. Figure 3.4 illustrates the metal deposition and liftoff. The n-type ohmic contacts were annealed for 30 s at 750° C using a rapid thermal annealing (RTA) furnace under $N_2$ gas for the interfacial reaction of the metal contacts.

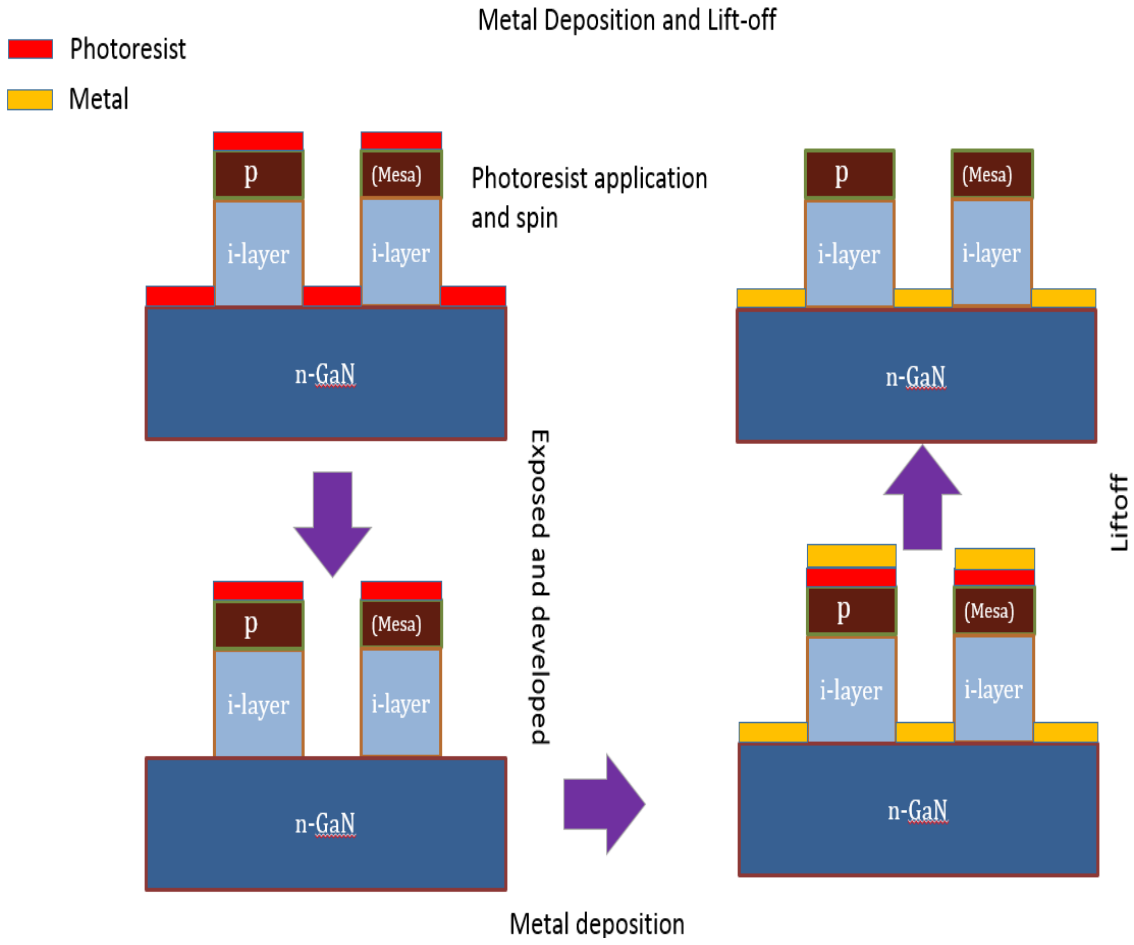


*Figure 3-4 Metal deposition and Lift-off*

### 3. Wire-bonding & Packaging

To form a pattern for p-type ohmic contacts, the sample was prepared in a similar manner as in step 1 except the p-type ohmic contact photomask was used. After the descum in metroline asher, the sample was wet etched in HCl for one minute to remove the oxide layer before loading it in the CHA for metal deposition. Ni/Au (500/1500 Å) was the metal stack deposited and liftoff was done in the same manner as in step 3. The sample was annealed at 500°C for 60 s in the RTA furnace in $N_2$ gas.

### 4. Wire-bonding & Packaging

In order to wire bond these devices to a 40-pin DIP (dual inline package), an extra layer of metal stack was evaporated using the 4th layer of the photomask. The samples were prepared for metal deposition similarly as in step 3 and Ti/Au (50/500 A) was the metal stack evaporated. After that, these devices were wire bonded to a DIP with thin Au wires using the wire bonder. Figure 3.5 shows the image of the wire-bonder. All the n-type contacts were interconnected (wire bonded to each other) and then connected to one of the pins on the package. All the p-type contacts were wire bonded individually and then were directly connected to a unique pin on the DIP.

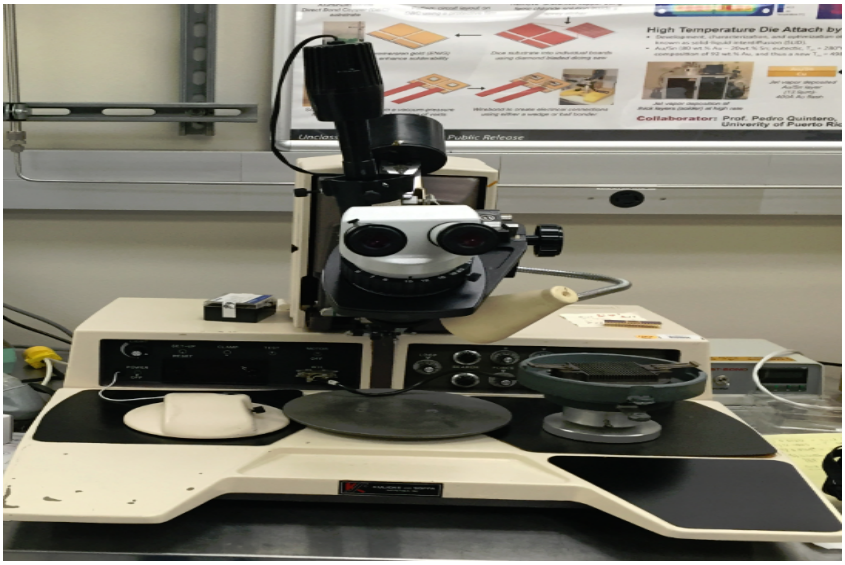


*Figure 3-5 Wire bonder*

*3.1 Depletion Region Width and Capacitance Calculations:*

An estimation of the width of the depletion region (W) for these devices can be calculated using equation 3.1, provided the equilibrium carrier concentrations of each layer are accurately known. The width of the depletion region at zero bias of a *p-n* junction is given by:

$$W = \sqrt{\frac{2\varepsilon_G}{q} V_{bi} \frac{(N_a + N_d)}{N_a N_d}} \qquad (3.1)$$

Where:

$N_d$ and $N_a$ are the concentrations of donor and acceptor ions, respectively.

$V_{bi}$ is the built in voltage given by

$$V_{bi} = \frac{KT}{q} \ln \left(\frac{N_a N_d}{Ni\text{^}2}\right) \qquad (3.2)$$

q is the electron charge = 1.6 x $10^{-19}$ C

K is the Boltzmann constant = 1.381 x $10^{-23}$ Joules/Kelvin

T = 300 K room temperature in Kelvin

$N_i$ = 1.9 x 10 $^{-10}$ cm$^{-3}$ is the intrinsic carrier concentration of GaN, at room temperature

$\varepsilon_G$ = 9.5 is the dielectric constant of GaN, and 8.85 x 10$^{-14}$ is the permittivity of free space in F/cm

Similarly, the capacitance at the pn junction can be determined by equation 3.3:

$$C' = \frac{q*E_{GaN}*Na*Nd}{(2(Vbi+VR)(Na+Nd))} = 1.4404\ x\ 10^{-8}\ \frac{F}{cm^2} \qquad (3.3)$$

The total capacitance at the junction is given by:

$$C = C'x\ A$$

Where A is the area of the device.

*3.2 Characterization:*

The devices were characterized using current - voltage (IV) measurements without illumination (light or beta), using a laser driven light source, and under an electron beam at various accelerating voltages to simulate their behavior as betavoltaic microbatteries.

3.3.1 IV measurements:

The fundamental component of a betavoltaic device is the semiconductor diode, which converts the kinetic energy of beta particles into electrical energy. The diode has a *p-i-n* structure. We performed current – voltage (IV) measurement on these devices to see if they show rectification. IV measurements were performed in a Wentworth PML 8000 probe station at room temperature using an Agilent 4155 semiconductor parameter analyze. Figure 3.6 shows the IV measurement set-up. The

devices were tested in a forward bias by sweeping the voltage from 0 V to 10 V. The current compliance was set at 85 mA to avoid destruction of devices through heating. In reverse bias, the voltage sweep was performed from 0 V to -10 V with the current compliance set at 1 mA to avoid destructive breakdown.

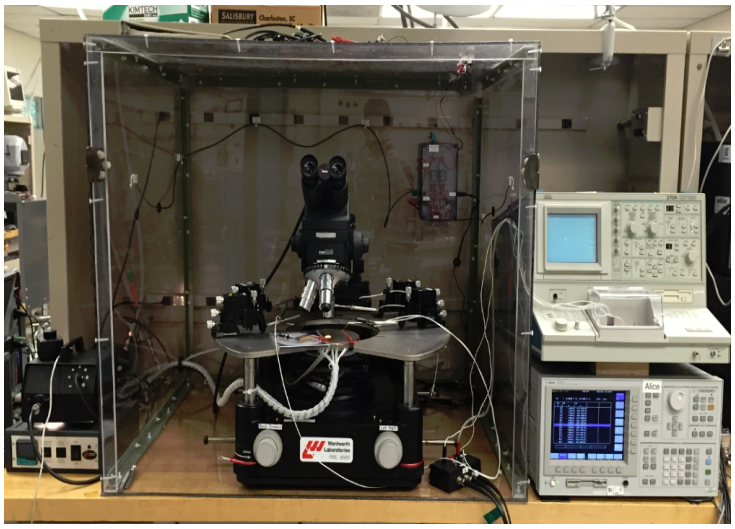

*Figure 3-6 IV measurement set-up*

The contact resistance was measured by performing the IV measurements on the transmission line method (TLM) structures as shown in figure 3.7. The TLM structures consist of seven 100 µm x 100 µm squares. The spacing between the squares are: 2.5 µm, 5 µm, 10 µm, 30 µm, 40 µm and 50 µm

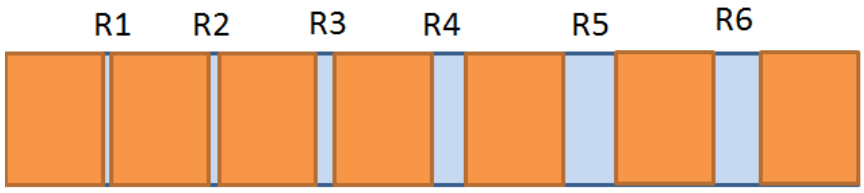


*Figure 3-7 TLM structures*

### 3.3.2 Photo-IV measurement

Since the working principle of a betavoltaic device is similar to a photovoltaic device, we characterized our devices under a monochromatic light source to see if they show a photoresponse. These measurements were taken similarly as to the dark IV measurements but a laser energy driven light source was incident on the devices when the voltage sweep was performed from -3 V to 3 V. The wavelength of the light source was set to 310 nm, which corresponds to photon energy of 4.0 eV (slightly higher than the bandgap of GaN). The data for the IV curves was generated using an external Keithly semiconductor parameter analyzer.

### 3.3.3 Electron beam measurements

Due to the dangerous nature of working with radioactive beta sources, an electron beam was used to emulate the behavior of these devices exposed to a beta source. The monochromatic electron beam's input current was fixed at 1nA and the voltage of it was varied from 1 kV to 16 kV. These measurements were taken similarly as to the photo-response measurements but an electron beam was used instead of a light source. An external semiconductor analyzer generated the IV curves as the electron beam was incident on the device. By doing this, we were able to simulate the behavior of these devices for tritium and nickel-63 beta sources.

The electron beam set up is shown in figure 3.8. It consists of an electron beam gun, a chamber, cryo pump and ion gauge reader. The sample is placed in the chamber and the pressure of the chamber is pumped to a vacuum ($2 \times 10^{-6}$ or below) using a cryo pump. The pressure readings are displayed on the ion-gauge reader.

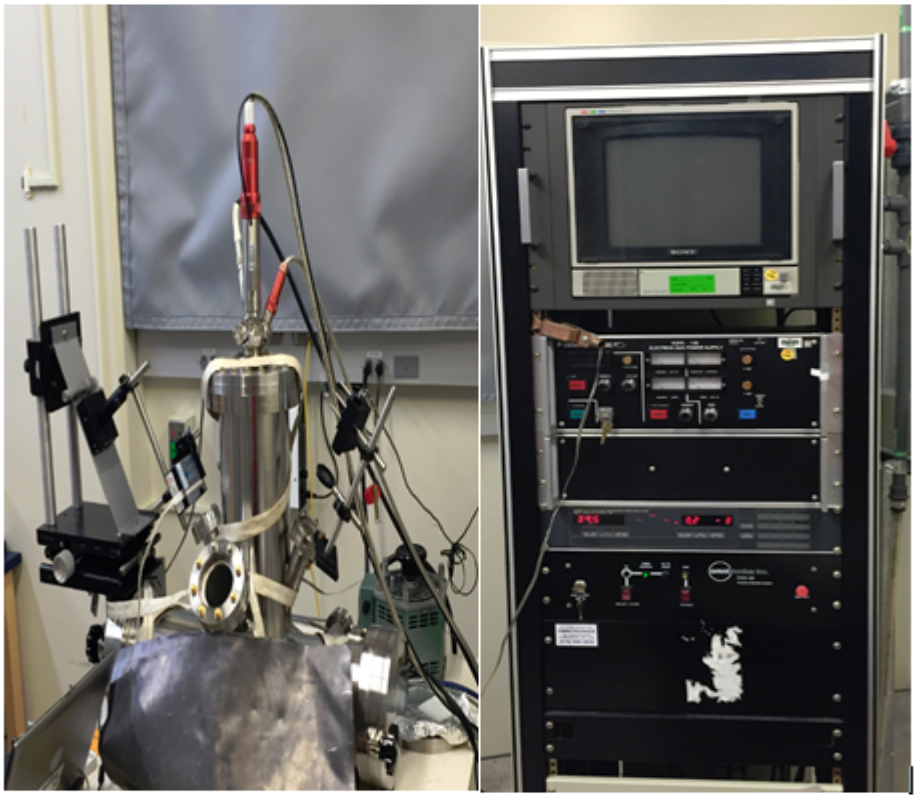

*Figure 3-8 Electron-beam measurement set-up*

3.3.4 Electron beam induced current (EBIC)

The EBIC measurements were performed to see the different regions of the device. This EBIC measurement set-up is shown in figure 3.9. In this set-up, an electron beam from the secondary electron microscopy (SEM) is scanned over the device to generate EHPs. The current created due to the collection of EHPs is measured using an external ammeter. An SEM image is taken simultaneously which differentiates between the areas of the device where generated EHPs are not collected to the areas where generated EHPs are collected and contribute to the current of the device. Figure 3.9 shows the image of the EBIC measurement set

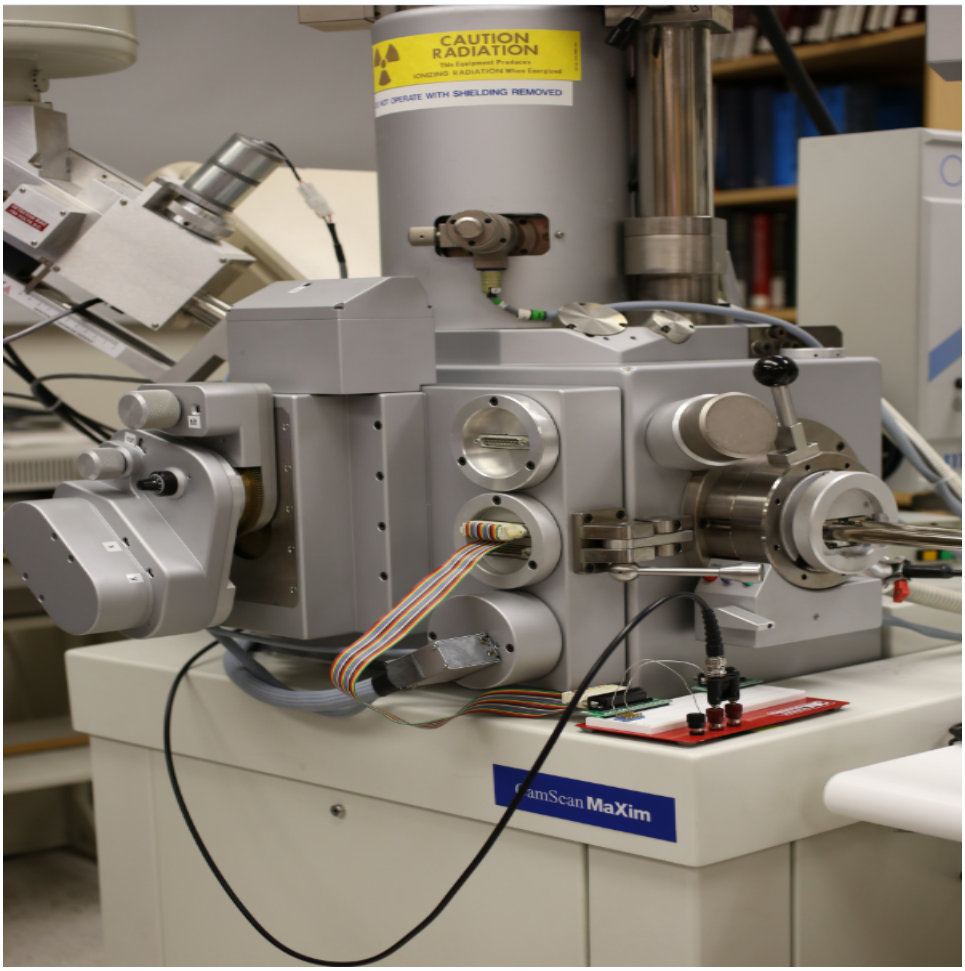


*Figure 3-9 EBIC measurement set-up*

# Chapter 4. Experimental Equipment and Procedures

This chapter lists all the equipment used in this work and provides a brief overview for each of the equipment used with an image.

## *4.1 MOCVD System*

The GaN sample was grown using a Veeco MOCVD system as shown in figure 4.1. MOCVD is an epitaxial crystal growth technique used to produce high quality semiconductor thin films with excellent scalability and high throughput. The most common application of MOCVD is in the production of compound semiconductor device structures for applications such as solar cells, laser diodes and light emitting diodes. Deposition is achieved through the reaction of an organometallic and hydride precursor gases in the presence of a heated substrate. In the case of GaN, the precursors are usually trimethylgallium (TMG) and ammonia ($NH_3$). The quality of the resulting films is dependent on precise control of the growth conditions, including temperature, pressure, gas flow rates, and precursor ratios. The choice of substrate also has a large impact on film quality, as is the case in all forms of epitaxy. Common dopants for MOCVD GaN materials include silicon for n-type and magnesium for p-type. Growth rates are generally on the order of ~ 2 μm/hr.


*Figure 4-1 MOCVD Reactor*

*4.2 Automated Dicing Saw*

The Disco Dads3240 automated dicing saw was used to dice the 2'' GaN wafer for this study as shown in figure 4.2. It is a very high precision tool used to cut semiconductor wafers into individual dies. A wafer is placed on a vacuum chuck to keep the sample from moving. The chuck accommodates circular and rectangular wafers in a range from 1" to 8". The dicing wheel is mounted on a high frequency air-bearing spindle with a variable rotation speed of 6,000 rpm to 60,000 rpm. The cutting feed speed of this tool is variable from 0.000 to 600 mm/sec. Following each cut, the Disco saw uses stored parameters to automatically index the wafer and make another cut until all the programmed cuts are completed.


*Figure 4-2 Dicing Saw*

## *4.3 Fabrication*

The equipment used in the fabrication process are: photomask writer, mask aligner, Inductively coupled plasma (ICP) etcher, Metroline Asher, CHA e-beam metal evaporator and rapid thermal annealing (RTA) furnace.

### 4.3.1 Photomask Laser Writer

The photomasks used in this study were designed using AutoCad and subsequent .dxf file drawings were transferred to mask plates using the Heidelberg DWL 66fs laser mask writer as shown in figure 4.3. The Heidelberg DWL 66fs is a high-resolution pattern generator for mask making. The system has three computers, one for converting user patterns to LIC files (Linux PC); one for setting up the

writing job (Windows PC); and one for executing the job (OS9, on board of the tool). It uses acousto-optic modulators to adjust the laser intensity, and acousto-optic deflectors to scan the beam. During an exposure, only the stage moves and the substrate is held down on the stage by vacuum and moves only in the x-y plane.

The optical setup utilizes a single-mode diode laser ($\lambda$ = 405 nm) as its light source. There are two write heads available: 5 mm & 20 mm. Both heads use an air-gauge to monitor the $N_2$ pressure change, which is then feedback to the lens piezo actuators for auto focus. During a scan, user patterns are divided into stripes along the Y-axis, each stripe contains 100 pixels. The stage moves along Y-axis to finish exposing one stripe, then steps in the X-axis to start exposing the next stripe. The user patterns are then stitched together. In terms of resolution, the 5 mm write head can achieve a minimum feature size of ~800 nm, the 20 mm head can achieve a minimum feature size of ~4 μm. The 20 mm head writes about 12 times faster than the 5 mm head.

The size of the mask plates used is 8 inches x 8 inches. After the laser exposure, the mask was first developed in AZ 400 for 60 s before a chrome etch for ~ 2 minutes. Then the PRS 3000 was used to remove the resist for ~ 5 minutes.

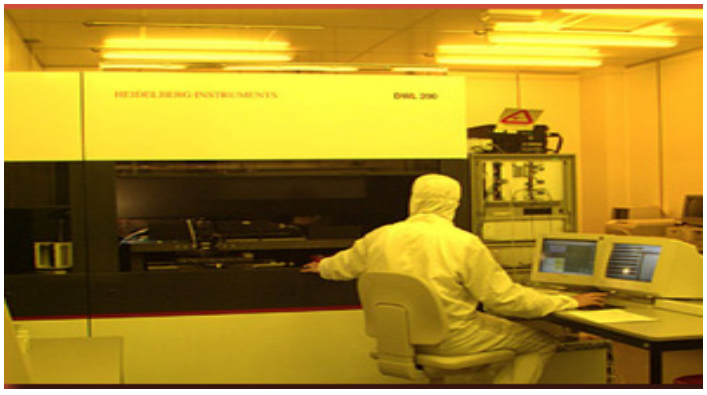

*Figure 4-3 Photomask laser writer*

### 4.3.2 Spinner and Hotplate

The spinner is used for spin-coating photoresist on the wafers. The spinner allows a user to set the spin speed, ramp time and time of the spin. The spin speed is an important parameter as it determines the resist thickness. AZ5214E is the resist used for this work. This resist can be used for both positive and negative applications. At 2000 RPM, a resist thickness of 2 μm was achieved. The hot plate is used to bake the sample and it can be set to a wide temperature range from 25 ºC up to 1000 ºC.

### 4.3.3 Mask Aligner

The Karl Suss MA6 mask aligner (figure 4.4) was used to align and expose the sample to transfer the device features from the mask onto the sample. The Karl Suss MA6 is a contact printer used for fine lithography for device features as small as 1 micron. It is capable of processing both 4- and 6-inch substrates. A 1000 W mercury arc lamp is used to expose the wafers. This lamp is capable of operating in constant power mode, or in constant intensity mode. Wafers are aligned to the mask using a conventional microscope located on the top. This tool allows 5 different contact modes or the force between the substrate and to the photomask before UV exposure: soft contact, hard contact, vacuum contact, low vacuum contact and proximity. For this work, hard contact was used. The flood exposure was also performed using this tool.

*Figure 4-4 Mask aligner*

4.3.4 Plasma Etcher

The sample for this work was etched using the Oxford ICP etcher as shown in figure 4.5. ICP is a dry etching technique that uses a plasma system to obtain anisotropic etching profiles, mainly to avoid the undercutting problem by wet etching. Plasma is formed by introducing several gases into the chamber in which RF current (13.56 MHz) is passed through a coil creating a magnetic field in order to fire the plasma. This time varying magnetic field is maintained after firing, thereby generating an electric field which confines electrons to a circular path, thus resulting in high plasma densities. A chuck (where the sample is loaded) is connected to a different RF source (13.56 MHz) to control the DC bias, and thus plasma power. This decoupling of the plasma power and plasma density reduces plasma damage, while maintaining high etch rates. Therefore, ICP is advantageous over other dry etch techniques such as RIE, where this does not occur.

The gases available in the Oxford ICP etcher at ARL are: Ar, $BCl_3$ , $Cl_2$ , $CF_2$, and $O_2$. This system is used for etching dielectrics, metals, and semiconductors. For this study, $BCl_3/Cl_2$/Ar plasma chemistry was used to etch GaN with power of 50 W, chlorine flow of 18 sccm, $BCl_3$ flow of 12 sccm, which corresponds to a system pressure of 10 mTorr.

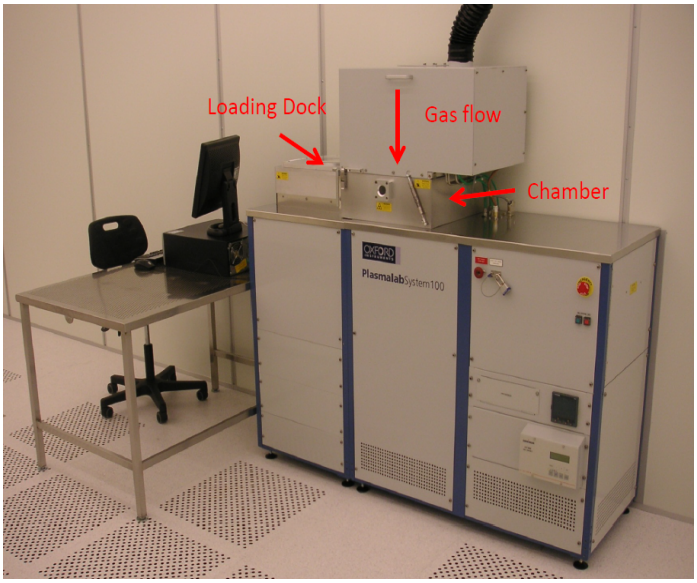


*Figure 4-5 ICP etcher*

4.3.5 Plasma Asher

The MetroLine M4L plasma asher was used to descum the sample. The purpose of descuming is to clean the sample from organics mainly created by the photoresist residue after the photolithography. Figure 4.6 shows the image of the metroline plasma asher.


*Figure 4-6 Plasma asher*

4.3.6 Electron-beam evaporator

The metal for ohmic contacts were evaporated using the CHA e-beam evaporator as shown in figure 4.7. The CHA Evaporator is an electron beam metal evaporator with the capability of coating eight 4-inch diameter wafers at a time. This tool enhances step coverage of the metal deposition by continuous modification of the landing angle of the evaporating metal atoms via a two-axis revolution/rotation substrate holder system (planetary mount). The CHA evaporator consists of a cryo-pump vacuum system that is designed to produce a low pressure vacuum and an electron gun producing a beam of electrons which impinge on a metal of choice for evaporating contained in a graphite crucible liner. The electron beam heats the metal in the crucible and creates a metal vapor inside the vacuum vessel and the vapor coats the wafers thus creating the metal coating. This system is supported with power supplies, valving and shutter controls, a viewing-port, and a material deposition sensor, which can measure the film thickness of the evaporated material.

*Figure 4-7 Electron-beam evaporator*

4.3.7 Rapid Thermal Annealer

The rapid thermal anneal (RTA) is a process tool (figure 4.8) used in the semiconductor device fabrication in which a single wafer is heated to a high temperature for a short amount of time in order to affect its electrical properties. Different heat treatments include: activating dopants, densify deposited films, change states of grown films, move dopants or drive dopants from one film into another or heating metal to form a better contact with the semiconductor. Unlike furnace anneals, RTA is short in duration (processing each wafer in several minutes) and the wafer is heated using a lamp based heating.


*Figure 4-8 Rapid thermal annealing furnace*

# Chapter 5. Results and Discussion

Figure 5.1 shows a cross sectional view of a fabricated betavoltaic device including details of epitaxial layers and the metal contacts. The n-GaN layer was exposed by selectively etching the p-GaN and *i*-GaN layers using an ICP etch. The n-type ohmic contacts consisted of an annealed Ti/Al/Ni/Au metal stack on the exposed n-layer. The p-type ohmic contacts were an annealed Ni/Au metal stack made on top of the mesa (*p-i-n*) structure as shown by the optical microscopy image in figure 5.2. Further fabrication details can be found in section 2 of chapter 3.

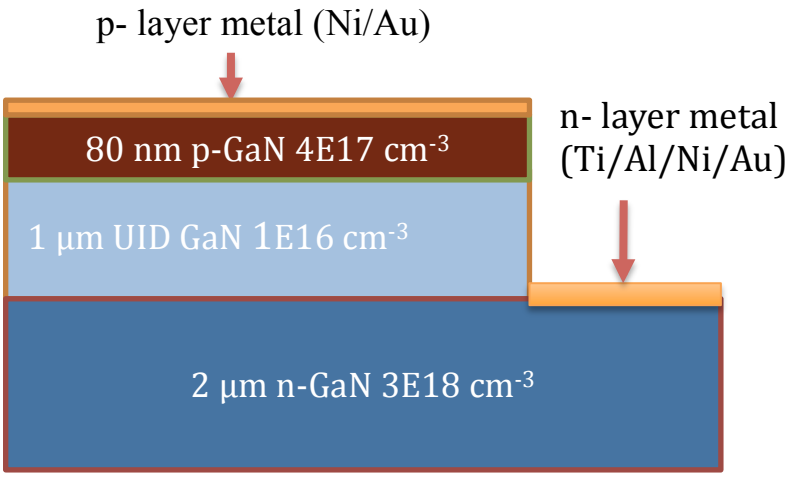


*Figure 5-1 device structure of a betavoltaic microbattery*

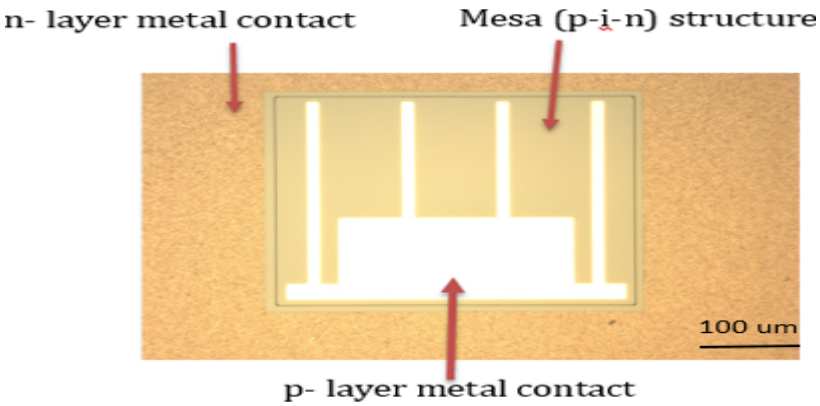


*Figure 5-2 Optical microscope image of the fabricated device*

After fabrication, the devices were wirebonded and packaged to a 40 pin dual inline pacakge (DIP). Figure 5.3 shows a secondary electron microscopy (SEM) image of the wirebonds in a packaged device. All the n-type contacts were wirebonded together and connected to one of the pins on the package. The p-type contacts were wirebonded individually and then directly connected to one of the pins on the package. Thus the devices are identified from their unique p-type ohmic contacts.

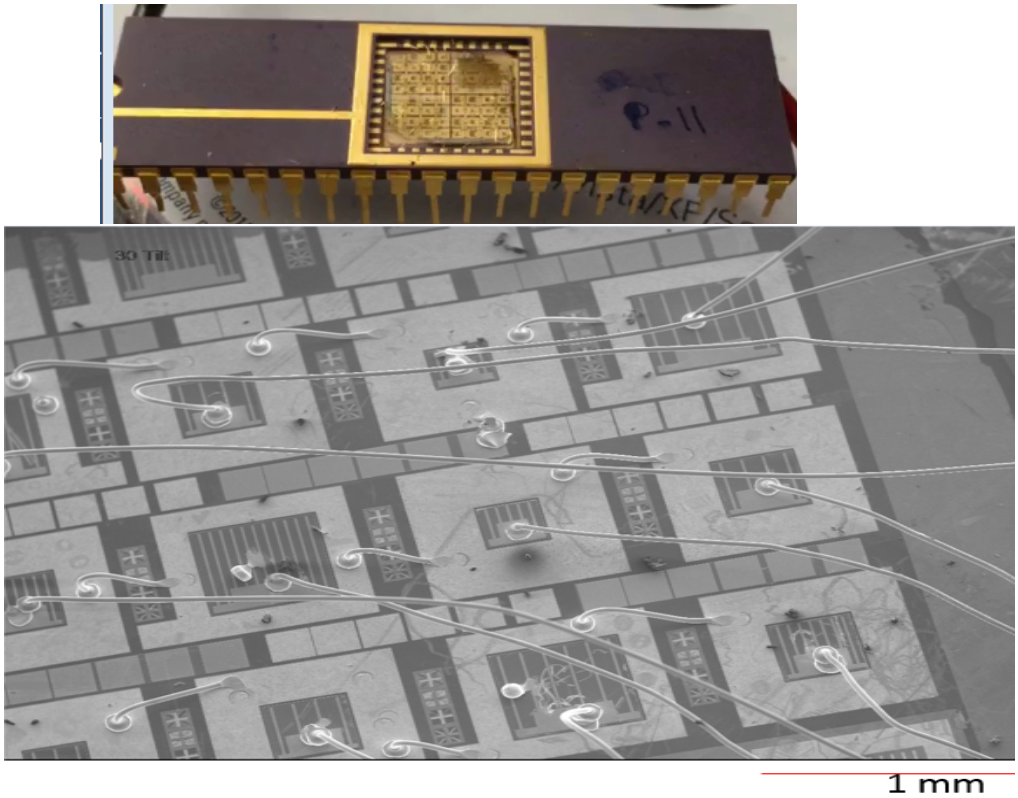


*Figure 5-3 (top) 40 pin DIP; (bottom) SEM image of the wire-bonds*

The width of the depletion region (W) for these devices was calculated using equation 3.1. $W_1 = 0.5836\,um$ was calculated in the first junction (between p-layer and the i-layer) and most of this depletion region exists in the low doped *i*-layer. However, in the second junction between i-layer and the n-layer, almost no depletion

region exists in the *i*-layer. From these calculations, we noticed that the two depletion regions do not overlap for our devices. Thus a part of the *i*-layer doesn't fully deplete and acts as a resistor because the *i*-layer of 1 μm is too thick to be fully depleted. The intrinsic layer of 1 μm was grown because we didn't know the carrier concentrations of each layer beforehand. The carrier concentrations were measured by the Hall effect measurements after the growth.

The contact resistance was measured by performing the current-voltage measurement using the transmission line method (TLM) structures on both sets of contacts as shown in figure 5.4.

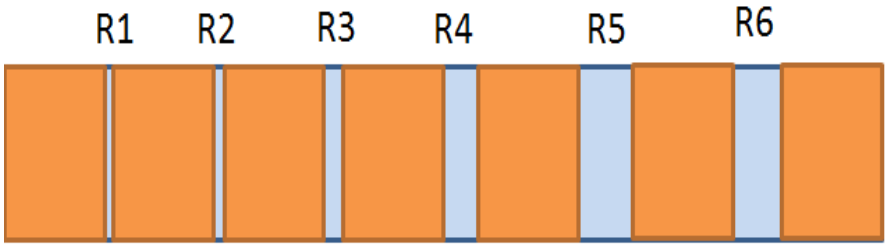


*Figure 5-4 TLM structure*

The contact resistance for the n-type ohmic contacts was measured to be $10^{-6}$ ohms-cm$^2$ and $10^{-3}$ ohms-cm$^2$ for p-type ohmic contacts. The ohmic contact made on the n-GaN has a contact resistance similar to what has been typically reported in the literature [38]. However, the contact resistance is a little higher for the p-type contacts compared to what's been typically reported ($10^{-5}$ ohms-cm$^2$) in the literature [39]. Our measured high p-type contact resistance is not surprising as it is a challenge to make low resistance ohmic contacts to p-GaN: the carrier concentration of p-type material cannot be increased to a degenerate level during epitaxial growth, and a practical metal with a larger work function than that of p-GaN is not available [39].

*5.1 IV Measurements*

Figure 5.5 shows the IV curves in the forward bias for 6 total devices where two devices of each size were tested. The IV curves in the forward bias show rectification as expected from a diode device and the turn-on voltage is roughly the same (~3.2V) for all devices. The turn on voltage is defined as the voltage at which the tangent to the IV curve in the "linear" region intercepts the voltage axis or simple the voltage at which the diode starts to conduct current.

Figure 5.6 shows the IV curves in the reverse bias for the same devices. Two out of 6 tested devices have high leakage currents. Device 11 (300 x 300 μm) reaches a current compliance of 1mA at -2.7 V and device 31 (600 x 600 μm) shows a leakage current of 1mA at -9V. This high leakage current is not dependent on the size of the devices; it's just that these two devices happen to have high leakage current that is likely caused by tunneling through defects in the p-n junction. The other 4 devices have low leakage current (~ 0.5mA at -10V) as shown below.

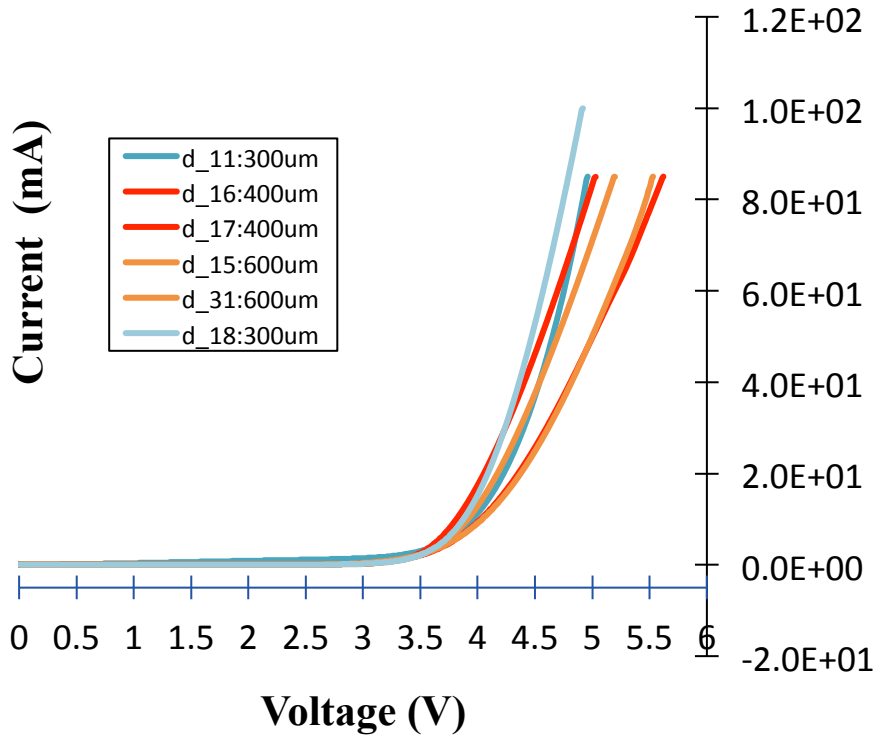


*Figure 5-5 IV cuves in Forward Bias*

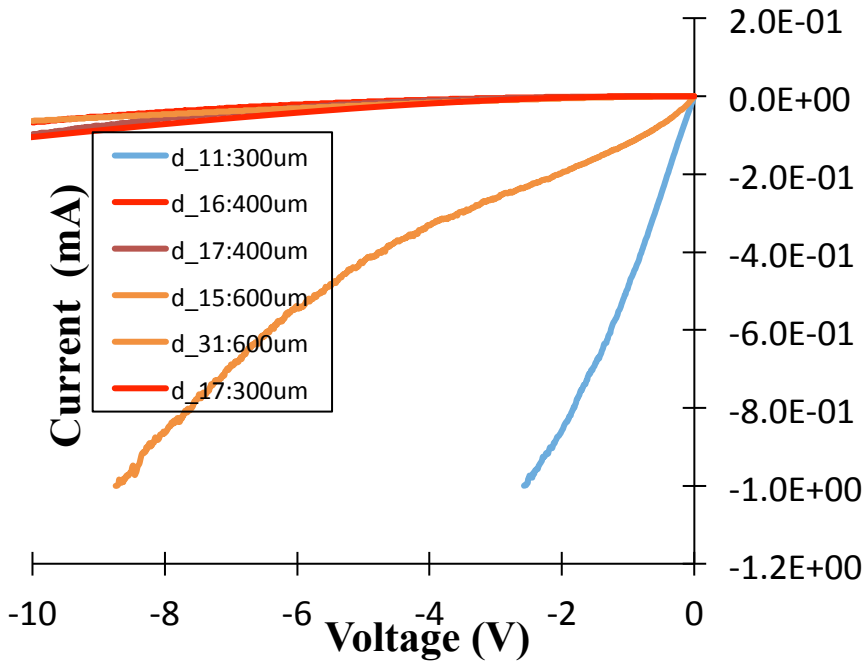


*Figure 5-6 IV curves in Reverse Bias*

Figure 5.7 shows the dark IV curves in the forward bias, but the current has a logarithmic scale. From these curves, we notice that there is a hump on all the IV curves at ~2.5 V. This hump is observed on all the IV curves and it is due to the fact that we have two junctions in our device because a part of the i-layer is not fully depleted.

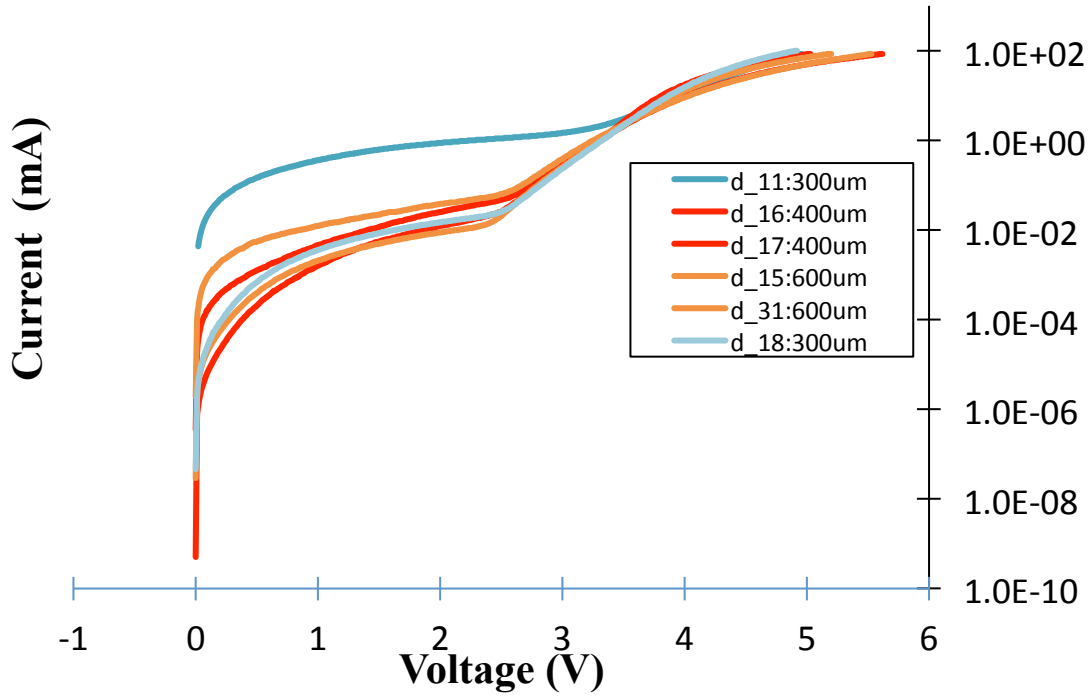


*Figure 5-7 log scale IV curves in Forward Bias*

The specific on resistance of all devices were calculated by fitting a linear line to the IV curves in the forward bias. Figure 5.8 shows the $R_{on}$ as a function of the area for all 6 devices that were tested.

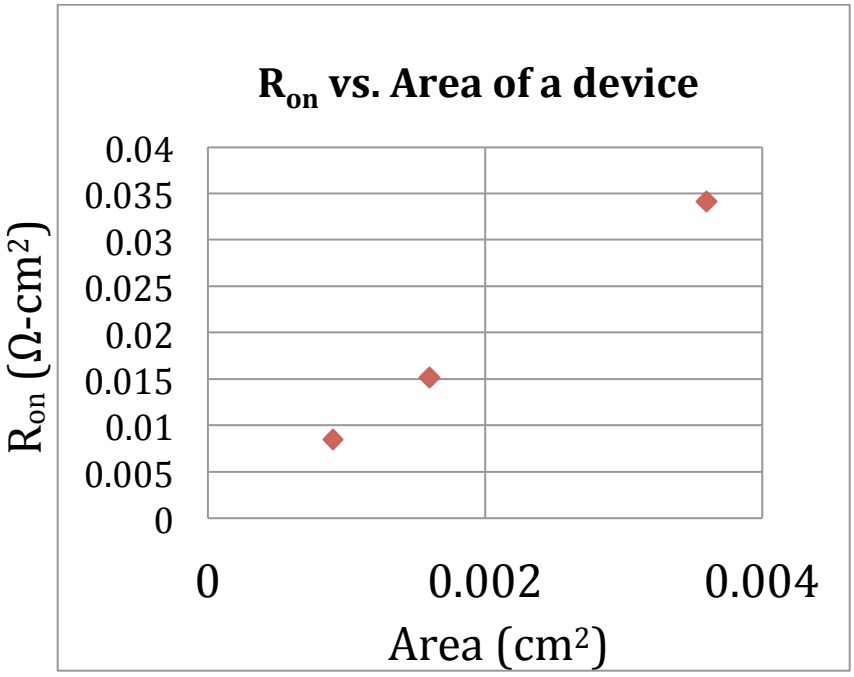


*Figure 5-8 specific on resistance vs area of a device*

The specific on resistance ($R_{on}$) was calculated to be 8.52 m Ω-cm$^2$, 15.15 m Ω-cm$^2$ and 34.09 m Ω-cm$^2$ for 300 x 300 µm, 400 x 400µm and 600 x 600 µm devices, respectively. The $R_{on}$ was averaged for two devices of each size. The specific on resistance takes into account the contact resistance, series resistance and the junction resistances present in the device.

During the dark IV measurements in the forward bias, we observed that these devices emit light (behaving as light emitting diodes) when the voltage sweep was performed from 0 to 10 V with the current compliance set at 85 mA. These devices begin to emit light slowly and as the bias voltage is increased, the devices begin to glow brigther and they turn off when the sweep is over at 10 V. Figure 5.9 shows the light emission from one of the devices in the forward bias. This light emitting behavior is expected under forward bias as GaN is a direct band gap semiconductor and the radiative recombination in the junction is dominant under forward bias. The

forward bias lowers the potential barrier between the n and p-layers, thus increasing te diffusion of carriers which recombine and generate a photon (light as shown in figure 5.9).

*Figure 5-9 Device operating as LED*

The IV results showed that four out of six devices have low leakage currents compared to the other two when operated in reverse bias. We decided to further characterize one of these four devices (device 17) with the photoresponse and electron beam measurements based on its better IV characteristics in the forward and reverse bias.

*5.2 Photo-response Measurement*

Figure 5.10 shows the photo-response of device 17 when tested under a laser driven light source with a wavelength of 310 nm. The IV curve dropped down to the fourth quadrant indicating the device is generating power, as opposed to consuming power. The device showed an open circuit voltage of 2.1 V and a short circuit current of -5.8 x $10^{-9}$ A. The maximum output power was calculated from the photocurrent curve as:

$$P_{max} = V_m * I_m$$

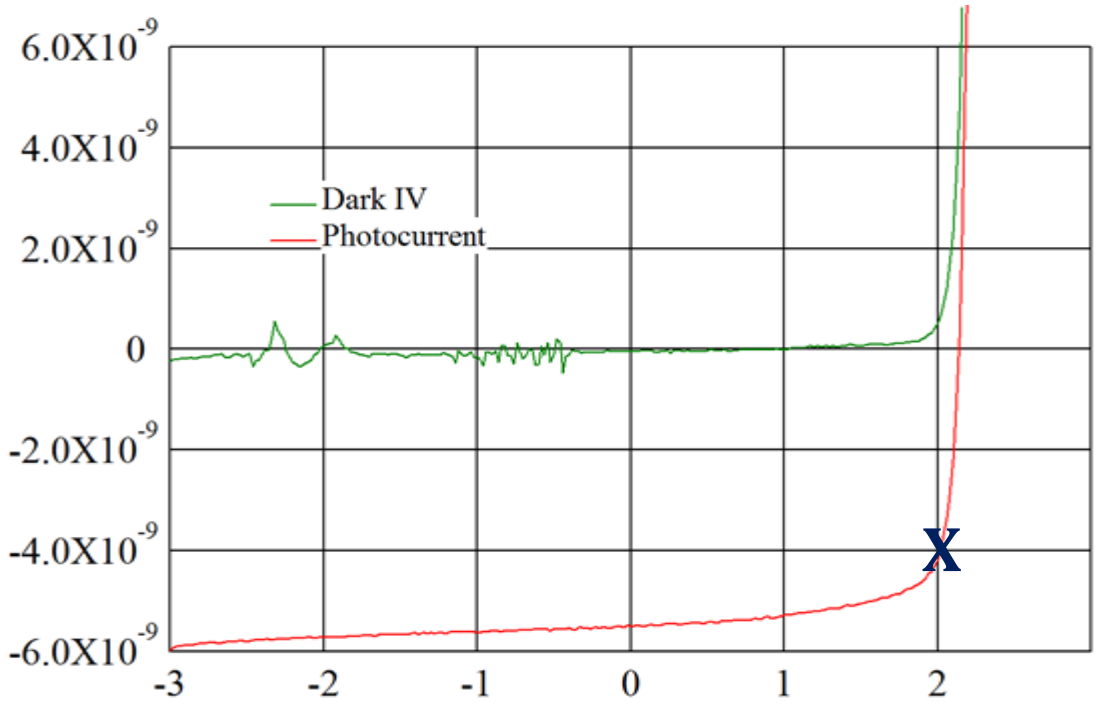


*Figure 5-10 photoresponse IV*

The fill factor (FF) of this device was calculated using equation 5.1

$$FF = \frac{V_m I_m}{V_{oc} I_{sc}} \qquad (5.1)$$

FF is a parameter which, in conjunction with $V_{oc}$ and $I_{sc}$, determines the maximum power from a solar device. $V_m$ and $I_m$ are the voltage and current at the maximum operating point of the device, respectively. Voc is the open circuit voltage and Isc is the short circuit current of a device. The fill factor of 0.693 shows that our device is a reasonable photovoltaic device.

*5.3 Electron-beam measurement*

Figure 5.11 shows the IV curves generated, as the electron beam was incident on device 17. The input current of the electron-beam was fixed at 1 nA and its voltage was varied from 1 kV to 16 kV with a step size of 1 kV. The IV current continuously

dropped down in the fourth quadrant as the electron-beam energy was increased. The output power of the device was calculated at each 1 kV increment and is shown in figure 5.11. We observed that the output power of a device increased as the input power of the electron beam increased. This is because more EHPs are created in the device as the input power of the electron beam increases, thus increasing the output power of the device.

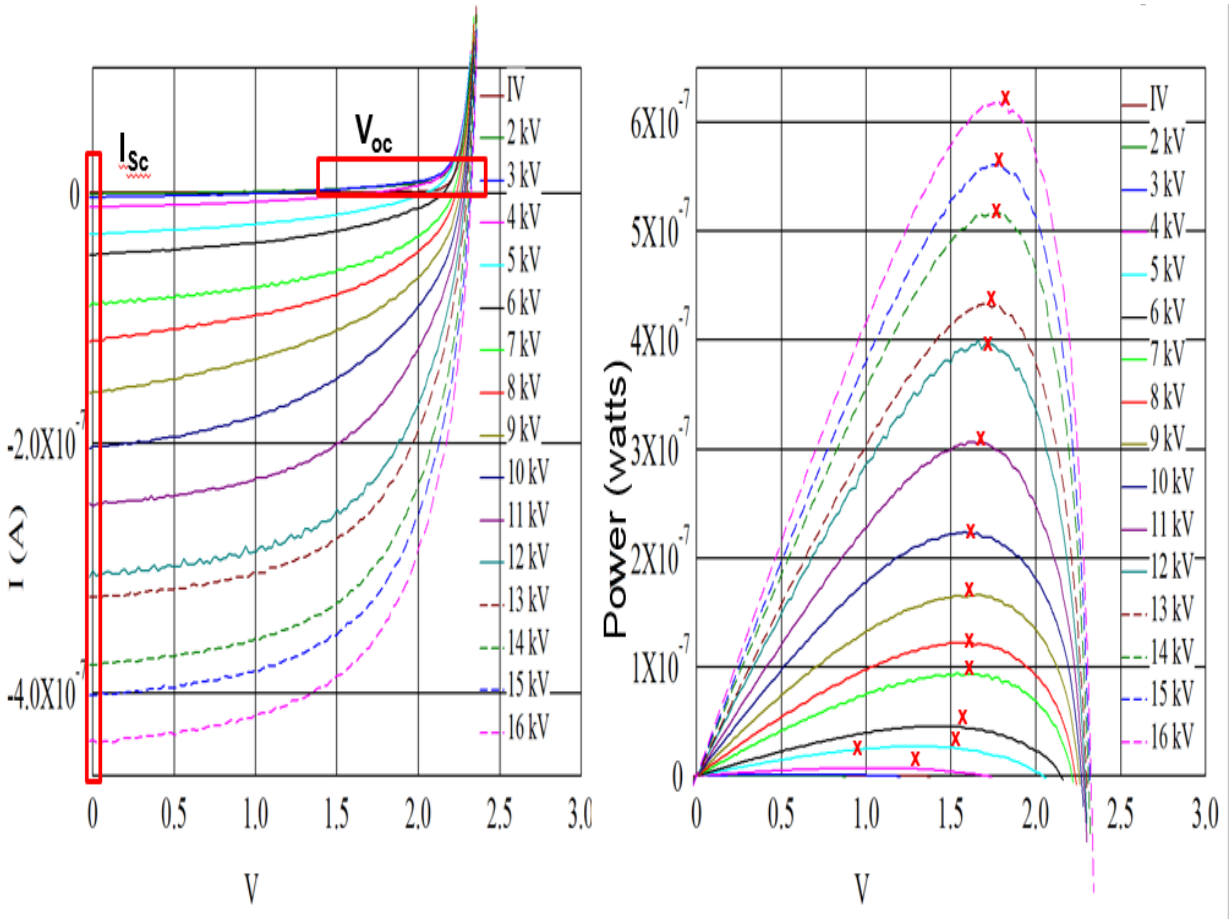


*Figure 5-11 a) IV curves as a function of voltage. b) the output power as a function of incident beam energy.*

Figure 5.12 shows the output power as a function of incident beam energy in keV. From this plot, we were able to calculate the output power at the average energy emission for beta sources $^{3}H$ and $Ni^{63}$. The output power of 70 nW was generated at

the average energy emission of $^{3}H$ (5.6keV) with an overall efficiency of 1.2% and the output power of ~640 nW at the average energy emission for $^{63}Ni$ (17 keV) with an overall efficiency of 4%. The overall efficiencies were calculated using equation 5.2.

$$\eta = \frac{P_{out}}{P_{in}} \qquad (5.2)$$

Where $P_{out}$ is the output power of the device and Pin is the total incident beam energy at that point of the output power. Our electron beam system has maximum electron energy of 16 keV and the output power and efficiency simulating $Ni^{63}$ was calculated at the incident beam energy of 16 keV instead of 17 keV.

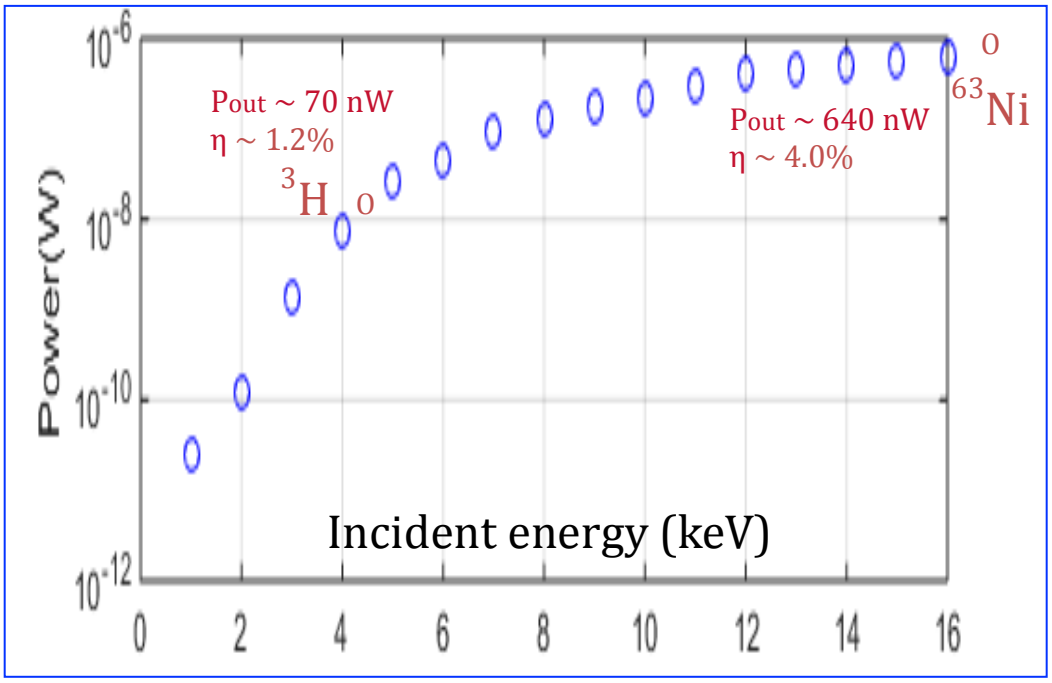


*Figure 5-12 output power as a function of incident e-beam energy.*

Figure 5.13 shows the $V_{oc}$ and $I_{sc}$ as a function of the incident electron-beam energy. We observed that the output power, $V_{oc}$ and $I_{sc}$ reaches a near constant value after ~7 keV. Thus, an increase in the incident electron energy does not significantly

increase the output power. The reason for this observation is that as the incident electron-beam energy is increased, the electron beam penetrates further into the material and generates more EHPs that are far below the depletion region. The EHPs that are generated far below the depletion region are not collected because they recombine before they are able to diffuse to the depletion region where there is no electric field there to sweep them out to their respective terminals. This phenomenon is shown in figure 5.14.

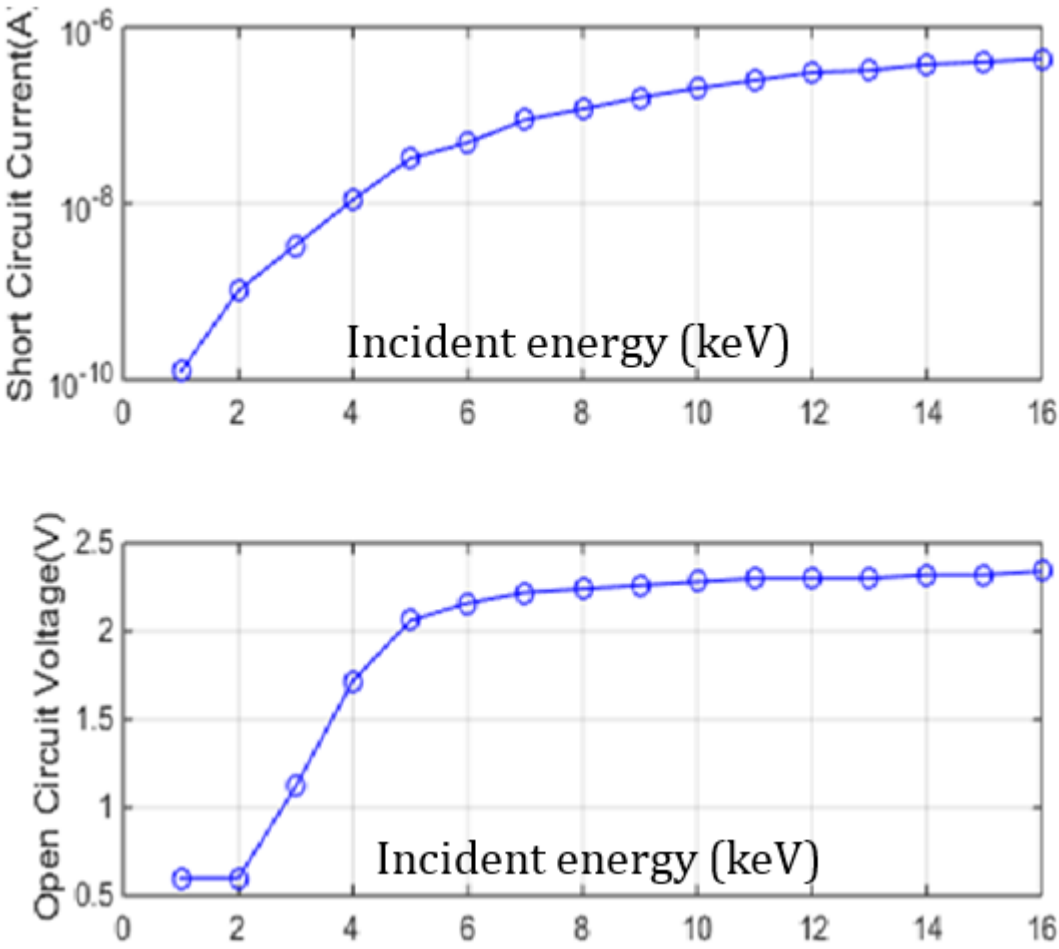


*Figure 5-13 $V_{oc}$ and $I_{sc}$ as a function of incident e-beam energy*

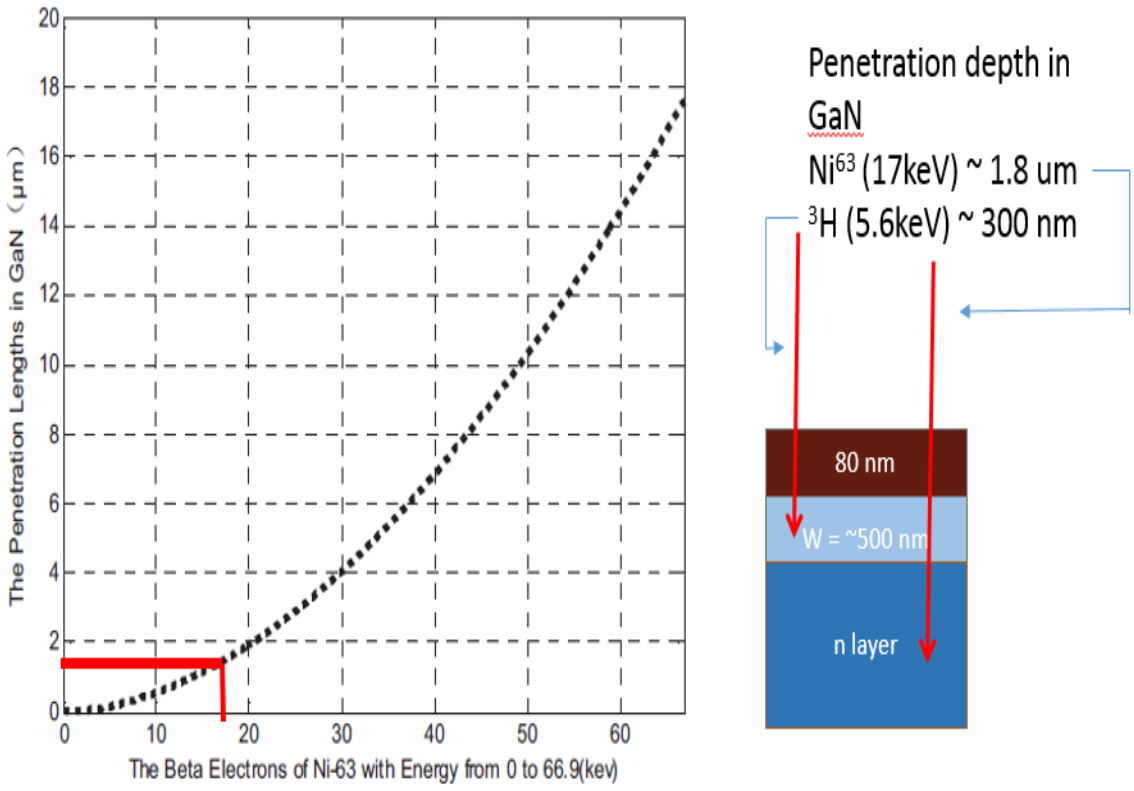


*Figure 5-14 Average electron penetration depth in GaN [36].*

*5.4 EBIC measurement*

Figure 5.15 shows the image of device#17 when electron beam induced current (EBIC) measurements were performed. In this measurement, an electron-beam (17 keV) from an SEM was scanned across the sample to generate EHPs in the device. Regions where more generated EHPs are collected and contribute to the total current have a higher intensity than regions with lower EHP collection. Regions with EHP collection are called the active region of the device. The maximum collection of carriers takes place in the *p-i-n* structure due to the presence of depletion region there and that's the region that has the higher intensity than any other region of the device. The n-contact is dark because EHPs are generated in that region, but they are not collected because the depletion region is not present there. The p-contact region is

brighter than the n-contact region, but not as bright as the p-i-n structure because the collection is attenuated in this region.

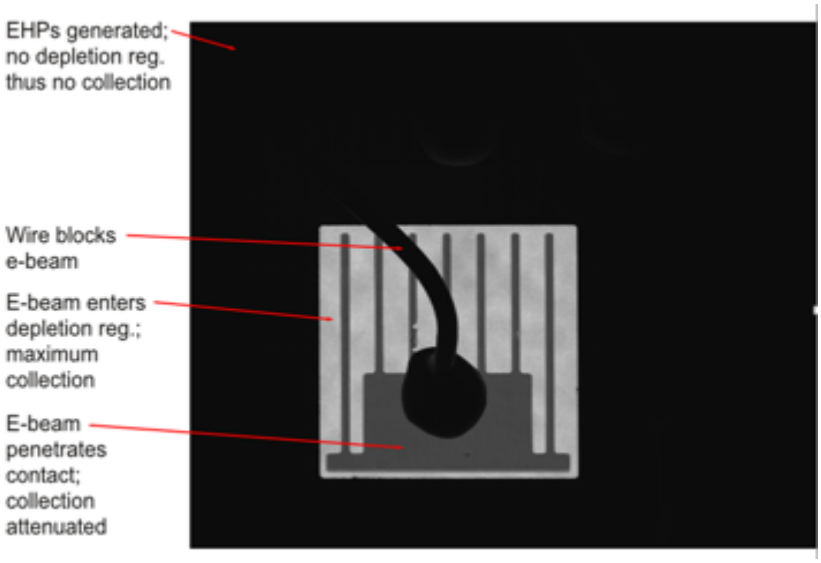


*Figure 5-15 SEM image showing EBIC*

# Chapter 6. Conclusion and Future Work

In this thesis, GaN based *p-i-n* devices are demonstrated for betavoltaic microbattery applications. A process was developed to fabricate and characterize these devices as betavoltaic microbatteries. Devices were fabricated on a GaN *p-i-n* (80 nm, 4.5 x $10^{17}$/1 μm, 1 x $10^{16}$ /2 μm, 1 x $10^{18}$) structure grown by metal organic chemical vapor deposition (MOCVD). The fabrication process was carried out in a class 100 cleanroom: photolithography, ICP etching and metallization. Thirty four devices were fabricated on a 1 cm x 1 cm sample. The devices had four different sizes, but the two largest (3.2 mm x 3.2 mm) devices did not function and were disregarded. However, the other devices of 3 different sizes behave as diodes showing rectification.

IV measurements in the dark (without beta/light illumination) were used to filter the devices that had high leakage current and/or large turn-on voltages for characterization under an electron beam in order to simulate their behavior as betavoltaic microbatteries. Two out of the 6 devices that were tested showed a high leakage current, independent of the size of the device. The leakage current in the other four devices was low, roughly the same in all of them (0.5 mA at -10 V). We chose one device (d_17, 400 μm x 400 μm) with the best IV characteristics in both the forward and reverse bias and tested it under an electron beam at various incident electron energies ranging from 1 keV to 16 keV. Output powers of 70 nW and 640 nW with overall efficiencies of 1.2% and 4.0% were generated from this device at the average energy emission of $^{3}$H (5.6 keV) and $^{63}$Ni (17 keV) beta sources, respectively.

Based on depletion width calculations and IV curves without illumination (beta/light), we determined that the *i*-layer of 1 µm was grown too thick to be fully depleted. Thus, increasing the specific on-resistance of our devices because the depletion region formed at the first junction (between p and i) did not fully extend all the way to the n-layer: a part of the i-layer was not depleted and this region behaved as a resistor, which reduced the output power and efficiency of our device.

## *6.1 Current and Future Work*

Based on the findings from this work, future work will involve doing the following to enhance the performance of GaN based betavoltaic devices.

1. A new photomask set has been designed to fabricate the betavoltaic devices. The p-contact area on the mesa (*p-i-n*) structure has been reduced on the new design, which ensures the entire beta particles incident on the device creates EHPs and no beta particle is reflected without creating the EHPs. The new mask has devices of two geometries (circular and squares) with the diameter size ranging from 200 µm to 100 µm. Two devices from the new photomask set are shown in figure 6.1.

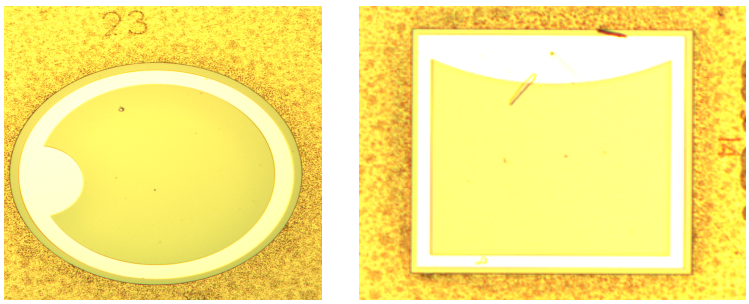

*Figure 6-1 Optimized device design*

2. The devices on GaN with optimized i-layer thickness (500 nm) are currently being fabricated using the new photomask set. These devices will be characterized as betavoltaic microbatteries and their performance will be compared to the GaN devices fabricated and characterized in this study.
3. The betavoltaic devices on AlGaN were successfully fabricated and are currently being evaluated as betavoltaic microbatteries. Their performance will be compared to conventional GaN betavoltaic devices. The film structure of the AlGaN sample is shown in figure 6.2.

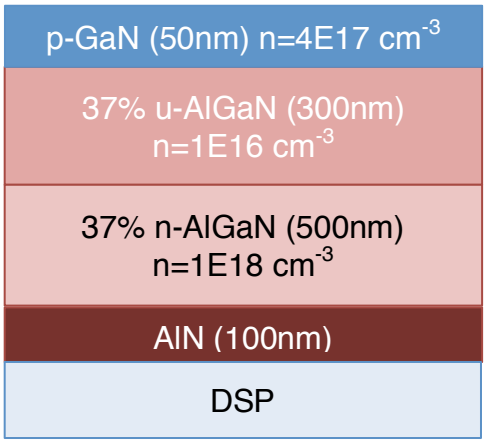


*Figure 6-2 AlGaN sample film structure*

4. Future research on GaN based devices for betavoltaic applications should entail GaN film structures grown on bulk GaN substrates because GaN films grown on sapphire substrate have higher threading dislocations (~ $10^{-9}$ $cm^{-2}$) compared to films grown on freestanding hydride vapor phase epitaxy (HVPE) GaN substrates (~ $10^{-6}$ $cm^{-2}$) or true bulk ammothermal GaN substrates (~ $10^{-3}$ $cm^{-2}$). These threading dislocations are caused by the lattice mismatch (~16%) between GaN films and the sapphire

substrate. Due to these threading dislocations, traps are found in devices, which cause a higher leakage current that reduces the output power and efficiency of betavoltaic devices made on GaN.

5. In order to enhance the performance of GaN based betavoltaic devices, a method has to be found to increase the width of the depletion region. One possibility could be to controllably dope the *i*-layer less than 1 x $10^{16}$ $cm^{-3}$ because as of today, the UID GaN layer cannot be doped lower than $10^{16}$ $cm^{-3}$. Thus, limiting the depletion width to approximately 500nm. Based on the doping levels given in figure 5.1, the i-layer should not be grown thicker than 500 nm: otherwise the specific on-resistance will be higher in devices.

# Bibliography


1. Wacharasindhu, T., et al., Liquid-semiconductor-based micro power source using radioisotope energy conversion. 2009.

2. Manasse, F., J. Pinajian, and A. Tse, Schottky barrier betavoltaic battery. IEEE Trans. Nucl. Sci, 1976. **23**(1).

3. Li, H., et al., Self-reciprocating radioisotope-powered cantilever. Journal of Applied Physics, 2002. **92**: p. 1122.

4. Duggirala, R., et al., Radioisotope thin-film fueled microfabricated reciprocating electromechanical power generator. Microelectromechanical Systems, Journal of, 2008. **17**(4): p. 837-849.

5. Chandrashekhar, M., et al., Demonstration of a 4H SiC betavoltaic cell. Applied Physics Letters, 2006. **88**: p. 033506.

6. Rybicki, G., C. Vargas-Aburto, and R. Uribe. Silicon Carbide Alphavoltaic Battery. 1996.

7. Bailey, S.G., et al. Photovoltaic development for alpha voltaic batteries. 2005: IEEE.

8. Christiana Honsberg, William A. Doolittle, Mark Allen, Chris Wang "GaN Betavoltaic Energy Converter" The 31st IEEE Photovoltaics Specialist Conference, Orlando Florida, January 3-7 2005.

9. W. Ehrenber, et al., "The Electron Voltaic Effect" Proc. Rody. Soc. 64, 424 (1951).

10. Rappaport, P., The electron-voltaic effect in p-n junctions induced by beta-particle bombardment. Physical Review, 1954. **93**(1): p. 246-247.

11. Pfann, W. and W. Van Roosbroeck, Radioactive and Photoelectric p n Junction Power Sources. Journal of Applied Physics, 1954. **25**: p. 1422.

12. Vul, B., et al., On the transformation of ß-particle energies to electric energy in germanium crystals with pn junctions. Atomic Energy, 1957. **2**(6): p. 653-657.

13. Olsen, L., S. Seeman, and B. Griffin, Betavoltaic nuclear electric power sources. Trans. Amer. Nucl. Soc., 12: 481-2 (Nov. 1969, 1969.

14. Ko, W. and J. Hynecek, Implant Evaluation of a Nuclear Power Source-Betacel® Battery. IEEE transactions on Biomedical Engineering, 1974: p. 238-241.

15. Huffman, F. and J. Norman, Nuclear-fueled cardiac pacemakers. Chest, 1974. **65**(6): p. 667.

16. Wei, L., Parametric studies and optimization of the beta-voltaic cell--I. Short-circuit current. Solid-State Electronics, 1974. **17**(10): p. 1091-1098.

17. Wei, L., Parametric studies and optimization of the beta-voltaic cell--II open-circuit voltage and power efficiencies. Solid-State Electronics, 1975. **18**(1): p. 71-77.

18. Guo, H. and A. Lal. Nanopower betavoltaic microbatteries. 2003.

19. Eiting, C., et al., Demonstration of a radiation resistant, high efficiency SiC betavoltaic. Applied Physics Letters, 2006. **88**: p. 064101.

20. Andreev V M, K E Bower, Y A Barbanel, Y G Shreter and G W Bohnert, Polymers, Phosphors, and Voltaics for Radioisotope Batteries, Boca Raton, FL: CRC Press, p 48 (2002).

21. Kyung-Ah Son, Anna Liao, Gerald Lung, Manuel Gallegos, Toshiro Hatake, Richard D. Harris, Leif Z. Scheick and William D. Smythe "GaN-based high-temperature and radiation-hard electronics for harsh environments", Proc. SPIE 7679, Micro- and Nanotechnology Sensors, Systems, and Applications II, 76790U (May 05, 2010); doi:10.1117/12.852711;

22. Look D C and Molnar P J, Appl. Phys. Lett., 70 3377 (1997).

23. Cheong M G, Appl. Phys. Lett., **77** 2557 (2002).

24. Zaijun Cheng, Xuyuan Chen, Haisheng San, Zhihong Feng and Bo Liu, J. Micromech. Microeng. **22** 074011(2012).

25. Zaijun Cheng, Haisheng San, and YanfeiLi, 5th IEEE International Conference on Nano/Micro Engineered and Molecular Systems, Xiamen, China (2010).

26. Krane, K.S. "Beta Decay." Introductory Nuclear Physics. New York,NY: Wiley, 1988. 273+. Print.

27. Shultis, J. Kenneth., and Richard E. Faw. "Radioactivity." Fundamentals of Nuclear Science and Engineering. Boca Raton: CRC, 2008. 96-100. Print.

28. Ferros, Angel. "β-dcay, the Neutrino Hypothesis, and the Special Theory of Relativity." Instituto De Investigaciones Electricas (n.d.)

29. Nuclear Physics PHY303 (PHY303 Nuclear Physics 8) < http://physics-database.group.shef.ac.uk/phy303/phy303-8.html >

30. R. B. Leighton, Principles of Modern Physics. McGraw-Hill Book Company, N.York, Toronto, London (1959).

31. Lutz, Josef. "Pin-Diodes." Semiconductor Power Devices: Physics, Characteristics, Reliability. Berlin: Springer, 2011. 159-66. Print.

32. Michael Shur, Physics of Semiconductor Devices, Prentice Hall (1990)

33. C. Klein, J. Appl. Phys., 39, 2029 (1968)

34. Neamen, Donald A. "The Pn Junction." Semiconductor Physics and Devices: Basic Principles. Boston: McGraw-Hill, 2003. 241-96. Print.

35. Kosteski, T., et al. Tritiated amorphous silicon betavoltaic devices. 2003: IET.

36. Cheng, Zaijun, Haisheng San, Yanfei Li, and Xuyuan Chen. "The Design Optimization for GaN-based Betavoltaic Microbattery." 2010 IEEE 5th International Conference on Nano/Micro Engineered and Molecular Systems (2010): n. pag. Web.

37. Blanchard, J., D. Henderson, and A. Lal, Nuclear Microbattery for MEMS Devices. U S. Deportment of Energy Award No. DEFG07-99ID13781. University of Wisconsin-Madison. Madison, WI. **53706**.

38. Fan, Zhifang, S. Noor Mohammad, Wook Kim, Özgür Aktas, Andrei E. Botchkarev, and Hadis Morkoç. "Very Low Resistance Multilayer Ohmic Contact to N-GaN." Appl. Phys. Lett. Applied Physics Letters 68.12 (1996): 1672. Web.

39. Ray-Hua et.al., “Low-resistance and high-transparency Ni/indium tin oxide ohmic contacts to p-type GaN” Appl. Phys. Lett.**79**, 2925(2001); http://dx.doi.org/10.1063/1.1415048